Photodegradation of disposable polypropylene face masks: Physicochemical properties of debris and implications for the toxicity of mask-carried river biofilms

Isabelle Bihannic, Renaud Gley, Lucas Gallo, Apolline Badura, Angelina Razafitianamaharavo, Maximilien Beuret, David Billet, Clément Bojic, Céline Caillet, Philippine Morlot, et al.

Photodegradation of disposable polypropylene face masks: physicochemical properties of debris and implications for the toxicity of mask-carried river biofilms

Isabelle Bihannic,[a,*] Renaud Gley,[a] Lucas Gallo,[a] Apolline Badura,[a] Angelina Razafitianamaharavo,[a] Maximilien Beuret,[b] David Billet,[a] Clément Bojic,[b] Céline Caillet,[a] Philippine Morlot,[b] Marie Zaffino,[b] Fatina Jouni,[b] Béatrice George,[c] Pascal Boulet,[d] Camille Noûs,[e] Michael Danger,[b] Vincent Felten,[b] Christophe Pagnout,[b] Jérôme F.L. Duval[a,*]

a. Université de Lorraine, CNRS, LIEC, F-54000 Nancy, France.
b. Université de Lorraine, CNRS, LIEC, F-57000 Metz, France.
c. Université de Lorraine, INRAE, LERMAB, F-54000 Nancy, France.
d. Université de Lorraine, CNRS, IJL, F-54000 Nancy, France.
e. Cogitamus Laboratory, Paris, France.

* Corresponding authors. Email: isabelle.bihannic@univ-lorraine.fr, jerome.duval@univ-lorraine.fr

Abstract.

COVID-19 outbreak led to a massive dissemination of protective polypropylene (PP) face masks in the environment, posing a new environmental risk amplified by mask photodegradation and fragmentation. Masks are made up of a several kilometres long-network of fibres with diameter from a few microns to around 20 microns. After photodegradation, these fibres disintegrate, producing water dispersible debris. Electrokinetics and particle stability observations support that photodegradation increases/decreases the charge/hydrophobicity of released colloidal fragments. This change in hydrophobicity is related to the production of UV-induced carbonyl and hydroxyl reactive groups detectable after a few days of exposure. Helical content, surface roughness and specific surface area of mask fibres are not significantly impacted by photodegradation. Fragmentation of fibres makes apparent, at the newly formed surfaces, otherwise-buried additives like TiO_2 nanoparticles and various organic components. Mortality of gammarids is found to increase significantly over time when fed with 3 days-UV aged masks that carry biofilms grown in river, which is due to a decreased abundance of microphyte therein. In contrast, bacteria abundance and microbial community composition remain unchanged regardless of mask degradation. Overall, this work reports physicochemical properties of pristine and photodegraded masks, and ecosystemic functions and ecotoxicity of freshwater biofilms they can carry.

Keywords. Polypropylene, Micro/nanoplastics, Freshwater biofilms, Algae, Gammarids mortality.

Environmental Implication.

As a legacy of COVID-19 pandemic, environments inherited new hazardous materials: polypropylene-based face masks and their secondary products generated by degradation. Scrutiny of their eco-impacts requires addressing how photodegradation -a dominant mask alteration process- mediates the interplay between physicochemical properties of masks (structure, composition and colloidal features of released debris) and their reactivity towards biota, in particular their colonization by freshwater biofilms and ensuing effects on consumers. Following a multiscale physicochemical approach in combination with ecotoxicity assays and onsite biofilm monitoring, this work sheds light on the photodegradation-induced properties and reactivity of masks under environmentally relevant conditions.

1. Introduction.

At a time when governments are legislating against the consumption of single-use plastic items, measures adopted to counteract the spread of COVID-19 pandemic led to a dramatic surge of plastic materials in our everyday life, in the form of packaging for protection purpose and personal protective equipment (PPE) like gloves and masks (Benson et al., 2021; Prata et al., 2020). As a result, the global daily production of masks - 90% of which are composed of polypropylene - was marked by a spectacular 30-fold increase from 2019 to 2020-2021, with 1 billion units per day (Prata et al., 2020; STATISTA, 2022). This massive production is not only explained by the needs to protect healthcare workers, but also by the recommendations and obligations formulated towards the society to wear masks in public places, medical centres and transports (Patrício Silva et al., 2020; WHO, 2021). The large use of personal protective equipment by the population is a new societal phenomenon, and it has now become a source of concern to treat and manage masks-related wastes beyond the specialized channels of the medical sector. The heavy constraints on waste collection channels, the overflow of treatment facilities and the behaviour of some consumers are all components of mismanagement of wastes and of their ensuing dispersion in e.g. rainwater, sewage networks, and natural environments (Ammendolia et al., 2021; Aragaw, 2020; Benson et al., 2021; Parashar and Hait, 2021; Prata et al., 2020). Realizing that most of the wastes ending up in oceans originates from a poor management, it is estimated that between 0.15 and 0.39 million tons of mask debris could end up in the global oceans on a yearly basis (Chowdhury et al., 2021). Noteworthily, whereas people were encouraged to wear face masks to avoid COVID-19 dissemination, a study highlighted recently the need to study long-term human-health risks associated with use of such protective equipment because face masks were evidenced to release fine particles and various (semi)volatile organic compounds (Guo et al., 2023).

The question then arises as whether the presence of masks in the environment can be assimilated to that of other 'conventional' plastic wastes. The answer is probably no, and masks along with their degradation products require a special attention for several reasons. Firstly, the general public in its majority does not necessarily know that masks and other disposable wet wipes do not degrade in the environment as easily as other cellulose-based materials would (Hu et al., 2022). Secondly, masks consist of fibres that are a few microns in diameter, which makes easier their breaking and fragmentation into micron-sized debris compared to other massive plastic objects. Another defining characteristic of masks is their large surface area, with strong implications in terms of e.g. adsorption of pollutants like metals or organics. Ma et al. (2022) reported that the surface area of a single mask is of the order of 1.4 m^2, which is 14 times larger than that of a 500 mL plastic bottle. In addition, based on mask fibre nature and size (cf. Ma et al. (2022)), PP density characteristics and considering a typical mass of a few grams for a mask (Saliu et al., 2021), it is easily estimated that the overall length of the fibres contained in the inner and outer layers of 3-ply masks can exceed a few kilometres and that it may even reach several hundred kilometres for the middle layer. Another important issue to consider when addressing the impact of masks dispersion and debris is the large spectrum of contaminants they can accumulate depending on places where degradation is operative, e.g. landfills, urban surfaces (sidewalks, gutters, parking lots) or road areas (Men et al., 2018).

Degradation of masks in the environment proceeds according to common plastic weathering processes, i.e. mechanical abrasion caused by wind and/or wave actions, UV radiation, oxidation in humid environments, or sea salinity-induced effects (Andrady, 2017; Gigault et al., 2018; Lambert and Wagner, 2016). For polyolefins (polyethylene and polypropylene), the most abundant polymers in

oceanic and freshwater environments, it is the action of solar UV that initiates photodegradation (Andrady, 2017), leading to material oxidation and breaking of polymer chains preferentially in amorphous areas. In turn, defects and cracks are produced, which favours fragmentation and the production of daughter particles. The generated fragments are qualified as secondary microplastics or nanoplastics if their size is below the micron scale (Gigault et al., 2018; Lambert and Wagner, 2016). Chemical modifications associated with photodegradation are accompanied by changes of the physical material properties, which includes size, porosity, density, crystallinity rate, surface charge or hydrophobicity. These properties further govern the reactivity of neo-formed colloidal particles (e.g. aggregation, buoyancy, etc.) and their interactions with aquatic organisms (Lambert et al., 2017). In literature, analyses of masks degradation consist generally in counting and characterizing debris spread by masks that were subjected to different ageing protocols intended to mimic environmental conditions, e.g. mechanical abrasion under dry conditions (Morgana et al., 2021), in fresh or salt water (Rathinamoorthy and Balasaraswathi, 2022), in the presence or not of sediments (Wang et al., 2021; Wu et al., 2022), following a first natural (Rathinamoorthy and Balasaraswathi, 2022) or artificial (Liu et al., 2022; Saliu et al., 2021) photodegradation step. All studies evidence the production of fibres and micro-fragments, in line with mask structure and literature results on polyolefin. Literature further suggests that photodegradation is the process that impacts most significantly the integrity of masks, with severe changes of their mechanical properties, modifications of their chemical groups (Liu et al., 2022) and increase of their hydrophilicity (Wang et al., 2021). We emphasize that, in literature, the signatures of chemical alterations of masks following photodegradation were found similar under natural and artificial conditions (Saliu et al., 2021).

Due to their size, nano- and microplastics - regardless of their origin (conventional wastes or masks) - can be easily ingested by many living species. The adhesion of nanoparticles on the surface of primary producers like microalgae has also been evidenced (Wright et al., 2020), together with their entry in the food chain (Chae et al., 2018). Whereas excretion processes may mitigate the extent to which some invertebrates accumulate plastics (Mateos-Cárdenas et al., 2020), impacts on their health have been reported, e.g. loss of mass, decreased growth and fertility, decreased mobility and/or increased mortality (Wright et al., 2013). The reasons for such adverse effects of plastics remain poorly understood, and various hypotheses have been formulated, i.e. false feeling of satiety, decreased ability to assimilate food due to dilution of available nutrients, or presence of lesions on- and inflammation of- the walls of digestive systems (Au et al., 2015; Blarer and Burkhardt-Holm, 2016). The response of organisms to plastics and residues thereof is most significant for fibrous shaped-particles due to the longer residence of these plastic fragments in the intestinal tract (Ogonowski et al., 2016), which disrupts severely cell metabolism and affects organism ability to process food (Au et al., 2015; Blarer and Burkhardt-Holm, 2016; Qiao et al., 2019). Toxicity of ingested microplastics may result from the action of their constitutive contaminants or the chemicals they carry, i.e. additives, catalysis residues, fillers (Oehlmann et al., 2009), or adsorbed pollutants (Felten et al., 2020).

To the best of our knowledge, most reports on nanoplastics have focused so far on polystyrene (PS) (Ferreira et al., 2019), whereas polypropylene (PP)-based materials like face masks received less attention despite of their abundance in the field (de Sá et al., 2018). This lack of studies on PP effects is partly explained by the large hydrophobicity of PP particles, which renders difficult their dispersion in aqueous medium, an issue that is often solved with the recourse to stabilizing surfactant agents of poor environmental relevance. There is however a strong connection between hydrophobicity of PP particles and their affinity to apolar contaminants, as illustrated by Rochman et al. (2013) who

evidenced large accumulation of polyaromatic hydrocarbons (PAH) et polychlorinated biphenyls (PCB) on PP particles under marine conditions. These elements advocate for further studies on PP plastic type, like surgical masks of central interest in this work. In addition, whereas studies have documented processes driving the degradation and release of PP masks debris, few of them comprehensively reported (i) the colloidal properties of these debris in terms of electrostatic charge, size and stability, (ii) how these properties are connected to conventional physicochemical descriptors of microplastic degradation evaluated by common microscopy and spectroscopy techniques, and (iii) whether or not ageing increases masks reactivity towards biota (toxicity issue). The assessment of surface features of released mask debris is also of particular interest not only because these debris develop a reactive surface area larger than that of conventional plastic waste, but also because they impact significantly on the fate, bioavailability and toxicity of aquatic contaminants like metals and organics and may act themselves as pollutants.

Accordingly, we report here a thorough characterization of the three layers composing disposable face masks using a suite of dedicated physicochemical techniques, from the molecular, colloidal to macroscopic scale. The physical, chemical and morphological information collected as a function of photodegradation treatment (mimicking solar degradation) are then discussed and compared with measured colloidal properties of released debris. A striking result inferred from this multi-technique assessment of mask degradation is that charged masks debris feature a moderate dependence of their colloidal features on duration of mask photodegradation. This contrasts with the marked macroscopic alteration of masks when exposed to UV radiation. Results therefore contradict the intuition according to which reactivity of debris generated by mask photodegradation is all the more important as UV exposure and macroscopic modification of mask properties are significant. We further address and discuss the extent to which physicochemical properties of aged masks, evaluated here across spatial and time scales, are relevant for defining (i) their capacity to host biofilm in freshwaters (Moselle River, Lorraine) and (ii) hazardous effects on the opportunist detrivore *Gammarus roeselii*. In detail, the objectives of this work are:

- **(a)** to address the physical-chemical properties of photodegraded masks - from the macroscopic down to the molecular scale and from the massive material to the generated colloidal debris - using a large spectrum of techniques (FTIR, AFM, DRX, elemental analysis, WAXS, SEM-EDS, electrokinetics, confocal imaging, gas adsorption, granulometry) detailed below. The analysis is performed for each constitutive polypropylene mask layer as a function of UV-exposure duration.
- **(b)** to analyze whether or not UV-mediated degradation of masks (and of their constitutive layers) - as specifically analysed in **(a)** - impacts the composition of biofilms grown on these masks once immersed in freshwater (here The Moselle River, France). The analysis is performed via examining the abundance and diversity of organisms found in river-biofilms grown on pristine, 1 day- and 3 days-aged masks, with the UV-aging process being realized prior to the immersion of masks in the river (cf. **(a)**).
- **(c)** to evaluate the toxicity of biofilms grown on undegraded and degraded masks (those biofilms are specifically generated and analysed in **(b)**) towards the opportunist detrivore gammarids *Gammarus roeselii.* The purpose is here to figure out the extent to which the river-biofilms (serving as food for gammarids) carried by the pristine and aged masks impact the survival of gammarids, i.e. whether or not mask aging process (and related biofilm composition, cf. **(b)**) leads/contributes to gammarids mortality.

2. Materials and methods.

2.1. Materials and photodegradation.

Disposable 3-ply surgical blue masks of the brand TD® Tidy Professional were made available by the French Ministry of Research and Education. These masks of type II (according to the EN14683 standard) are composed of three polypropylene (PP) layers. The white inner and blue outer layers (hereafter denoted as IL and OL, respectively) consist of spun-bound non-woven fabric, with 25 g/m² and 18 g/m² weights, respectively. The intermediate or middle PP layer (ML in short) is made of white meltblown fabric (20 g/m²).

Samples were subjected to ageing for 0, 1, 2, 3 and 28 days in a QUV tester (Q-Lab, USA) equipped with UV-A 340 lamps delivering an irradiation of 0.68 W/m²/nm. In this work, we selected the 'Standard practice for fluorescent UV exposure of plastics' (ASTM-D4329) to perform mask aging following Cycle A of that standard. Each Cycle A of 12 hours consisted in a first UV exposure period of 8 hours at 60°C, followed by a 4 hours condensation period in dark at 50°C. Prior to exposure, mask ties and nose bridges were removed, and test specimen were cut into 14 cm×8 cm pieces. Exposed surface of the layers was 6 cm×9 cm. After the UV-exposure period, masks were disassembled and layers were sorted according to their IL, OL and ML origin. Subsequently, layers were stored in dark at 15°C prior to further analysis. The nomenclature adopted to name analysed samples was defined according to: name of the layer (IL, OL or ML) followed by UV exposure duration, e.g. IL28d stands for inner mask layer exposed to UV for 28 days. Pristine samples, i.e. samples that were not subjected to UV treatment, were named ILp, OLp or MLp.

2.2. Physicochemical methods for characterization of mask material.

Chemical elemental analysis. Pristine samples were characterized in terms of their elemental composition of inorganics by Inductively Coupled Plasma Mass Spectrometry (ICP-MS). Pristine masks were analysed by the SARM laboratory (Service d'Analyse des Roches et des Minéraux, Nancy, France) using an ICP-MS iCapQ instrument. Samples were prepared by microwave-assisted acid digestion in quartz vessels using HNO_3-H_2O_2 solutions, following a procedure adapted from Muller et al. (2016) and Pereira et al. (2016). We placed 80 to 100 mg of mask layer material in a quartz vessel containing 1 mL (30% concentrated) H_20_2-2 ml (65% or 14 M) HNO_3 mixture. This mixture was then positioned in a microwave digestion chamber (UltraWAVE ECR by Milestone). Digestion was conducted under maximal N_2-pressure of 60 bars at 240 °C temperature.

Wide Angle X-ray Scattering (WAXS). In order to derive information on phase composition and degree of masks crystallinity depending on photodegradation level, WAXS data were collected on a Bruker Kappa Apex II diffractometer equipped with a mirror monochromator and a Cu Kα microsource (λ=1.5406 Å). Measurements were recorded in transmission mode on a two-dimensional detector placed at a 0.065 m distance from the samples. The reader is referred to **Appendix A** for details on data acquisition, evaluation and analysis of WAXS diffractions curves. Following a procedure available elsewhere (Goikhman et al., 1984; Isasi et al., 1999; Kotek et al., 2004; Lima et al., 2002), for each analysed sample we estimated a crystalline index (denoted as CI_X) defined by the ratio between area under the peaks corresponding to all crystalline phases and total area under the entire WAXS curve.

Fourier Transform Infrared spectroscopy (FTIR). To get insight into chemical composition of pristine and photodegraded mask materials, FTIR spectra were collected using a BRUKER VECTOR 22 spectrophotometer operated in transmission mode between 400 and 4000 cm^{-1} with 4 cm^{-1} resolution. Fifty scans were averaged per spectrum. The reader is referred to **Appendix A** for details on samples preparation. Effects of sample oxidation due to UV treatment were monitored according to the procedure by Almond et al. (2020). Namely, we evaluated a carbonyl index, denoted as CaI_{IR} and defined by the ratio between band areas corresponding to C=O carbonyl group (1850 to 1650 cm^{-1})

and methylene group (1500 to 1420 cm^{-1}). Prior to signal integration, linear baseline was subtracted from the signal in the 2000 to 740 cm^{-1} range. The helical content, denoted as HC_{IR}, was further derived from FTIR data after proper baseline correction (Hughes, 1969). HC_{IR} corresponds to the ratio between absorbances measured at 998 cm^{-1} and 973 cm^{-1} and it reflects the extent of polymer ordering, i.e. the amount of chains with helical conformation found in the isotactic domains (Blais et al., 1972; Luongo, 1960).

Scanning electron microscopy (SEM). Pieces of masks were imaged on a TESCAN VEGA scanning electron microscope (SEM) operating at 10 kV voltage. SEM set up was coupled to a Bruker XFlash6® 30 mm^2 EDS detector for energy dispersive X-ray spectroscopy (EDS) measurements. Square pieces were cut from materials with sufficient mechanical cohesion (relevant to pristine mask layers, to IL3d and OL3d samples). These pieces were then fixed with double-sided carbon tape on metallic sample holders. For most degraded samples, tape covered pads were dipped into powder of mask debris and cleaned gently with pressurized air to remove non-adhered materials.

Gas adsorption. The specific surface areas (SSA) of the pristine and 28 days-exposed masks were determined from krypton adsorption-desorption isotherms measured at 77K on a BELSORP-max II instrument (MicrotracBEL Corp.) following a step-by-step point acquisition method. The reader is referred to **Appendix A** for details on measurement procedure and evaluation of SSA using Brunauer-Emmet-Teller (BET) equation (Brunauer et al., 1938)**.**

Atomic Force Microscopy (AFM). To address surface topography of mask samples, AFM experiments were performed on a FastScan Dimension Icon equipped with a Nanoscope V controller (Bruker). AFM imaging was carried out using contact mode at ambient temperature in air. The reader is referred to **Appendix A** for details on samples preparation and adopted AFM probes. Surface roughness of fibres was estimated on XY images using Bruker NanoScope Analysis software (version 1.9). Roughness calculations were based on the entire images of the upper surface of cylinders laid lengthwise on the support. As fibres featured curved surfaces, flattening procedure was applied before roughness estimation. The entire images we considered for roughness evaluation consisted of 5-micron squares for the inner and outer layers and 2-micron squares for the middle one. All squares were 256 by 256 pixels. Two parameters defining roughness were computed: R_a and R_q that correspond to the arithmetic average of profile height deviations from mean surface, and the root mean square of these deviations, respectively. For the inner pristine layer, R_a and R_q were calculated on the basis of a single image. For the other layers analysed and conditions investigated, R_a and R_q calculations correspond to an average over two or three images.

Electrokinetics (electrophoresis). To address electrostatic properties of masks debris, their electrophoretic mobility (μ) was measured by micro-electrophoresis instrument (Zetaphoremeter IV, CAD Instrumentations, Les Essarts le Roi, France) in a quartz cell at 24°C as a function of salinity and pH of electrolyte solution, cf. details in **Appendix A**. The technique consists in measuring the velocity of charged particles suspended in an electrolyte solution under applied electric field condition (800 V m^{-1}). Displacements were converted into electrophoretic mobility with CAD image analysis software. Mask debris were dispersed in a 'very soft' water (cf. details in **Appendix A**) at final 0.225 g L^{-1} concentration. Conversion of μ into zeta-potential value requires application of available theories whose validity domains strongly depend on particle size and charge, particle nature (i.e. permeable or not to ions and/or electroosmotic flow developed under electrophoresis measuring conditions) and electrolyte concentration (cf. recent review by Gopmandal et al. (2022)). Accordingly, we did not proceed here to such a conversion.

Granulometry. After measurement of electrokinetic properties, particle size distributions were evaluated by laser diffraction granulometry (Malvern Panalytical Mastersizer 3000 instrument). For that purpose, 80 mL of the suspensions used for electrophoresis were dispersed in the very soft water medium described in **Appendix A** to reach a final volume of 400 mL. Size distributions were then evaluated from average of 3 measurements of ten seconds duration each. As investigated particles were anisometric, number- rather than volume-distributions were reported.

Confocal scanning laser microscopy. To visualize fibres of pristine and photodegraded masks in three dimensions on the basis of their defining fluorescence properties, we used confocal scanning laser microscopy (CLSM). CLSM images were recorded on a ZEISS Axio observer 7 microscope, equipped with a scanning head LSM 880. Pristine samples and 28 days UV exposed samples were placed in glass bottom dishes for visualization. Images of autofluorescence were recorded using a 561-nm diode laser for excitation. Emitted fluorescence was detected in the 570 to 694 nm wavelength range.

2.3. Formation of river-biofilms on pristine and photodegraded masks.

Experimental setup and sample collection. Pristine masks and masks photodegraded for 1 or 3 days (termed 1d and 3d masks, respectively) were placed in the Moselle River (49.282881 N 6.187556 E - Lorraine, France) for biofilm colonization. To that end, masks were maintained between two transparent polymethyl methacrylate sheets with an opening in the upper sheet to allow mask colonization by microorganisms. The experimental device was weighted and immersed horizontally at the edge of the river at a depth of ca. 1 m (**Appendix B, Figure B.1**). Masks were collected on May 19th, 2021 after 4 weeks immersion. They were gently rinsed with sterilized water to remove non-adherent microorganisms and transferred to laboratory for analyses. Depending on planned experiments, samples were either used freshly or stored at -20°C. On the same experimental site, alder leaves (*Aulnus Glutinosa* (L.)) were also conditioned by microorganisms for 10 days and served as controls of the experiments involving gammarids (cf. details below). A period of 4 weeks was selected for the immersion of masks for two main reasons: (i) the low microbial density typical of water column in Moselle River at the spring season, and (ii) the need to have a sufficient microbial biomass on masks so as to support toxicological experiments involving gammarids.

DNA extraction. Frozen masks were cut according to 1 cm diameter discs with a cork borer. Discs were then placed in a 2 mL tube and cut with scissors into small pieces for DNA extraction. DNA was extracted using the PowerSoil DNA Isolation Kit (MOBIO Laboratories, Carlsbad, CA) according to manufacturer's recommendations. The total amount and purity of DNA were determined by spectrometry at 260 nm and 230 nm using a NanoDrop spectrophotometer.

16S rRNA gene quantification**.** The abundance of bacterial 16S rRNA genes was estimated by qPCR using primers 968f and 1401r (Felske et al., 1998), and the reader is referred to **Appendix A** for related experimental details. For quantification, samples and standard plasmid dilutions were run in triplicate on the same plates. Quantitative PCR used a Step One Plus Real Time PCR system (Applied Biosystem).

Library construction, sequencing and data processing. Extracted DNA samples (4 replicates) were sent to Microsynth AG (Balgach, Switzerland) for sequencing. This company provides sample quality control and Nextera two-step PCR amplification using primer set 515f/806r targeting the V4 region of 16S rDNA (Klindworth et al., 2013), PCR product purification, quantification and equimolar pooling. Then, PCR libraries were sequenced on an Illumina MiSeq platform using a v2 500 cycles kit. Downstream processing including demultiplexing, merging, primer removal, quality filtering, trimming of Illumina adaptor residuals, chimera removal, operational taxonomic unit (OTU) clustering and OTU assignments were performed by Microsynth. Raw sequence files are available on the NCBI Short Read Archive (SRA) database under BioProject ID: PRJNA997609 and accession numbers: SAMN36684029 to 36684040.

Taxonomic identification of phytoplankton. Algal counting and identification analyses were performed with an inverted microscope (ZEISS Axiovert A1) following the Utermöhl method (Lund et al., 1958) at 400× magnification. For each sample, at least 400 individuals (filaments, colonies, and single-cell organisms) were enumerated and results were expressed in term of abundance of coenobes (coenebes mL^{-1}).

Confocal scanning laser microscopy (CSLM on colonized masks). After their immersion in Moselle River, mask samples were observed with a confocal scanning laser microscope (ZEISS LSM 880) in order to visualize deposited materials. Autofluorescence of the different masks' components was recorded using three different channels in a line sequential acquisition mode. Channels were set using the following parameters. Channel 1: Excitation at 488 nm – Emission from 499 to 570 for Channel 1. Channel 2: Excitation at 561 nm – Emission from 570 to 632 for Channel 2 (this channel corresponds to the mask fibers autofluorescence, cf. *Confocal scanning laser microscopy in §2.2*). Channel 3 corresponded to chlorophyll autofluorescence with an excitation at 633 nm and an emission recorded between 641 and 694 nm. The colour code adopted for the images of each channel corresponds to the median detection wavelength in that channel.

2.4. Assessment of pristine and photodegraded masks toxicity.

Biological material collection. *Gammarus roeselii* were collected with a hand net in La Nied River (Remilly, north-eastern France, 49°00'N and 6°23'E). The animals were placed in plastic coolers and transported within 30 min to the laboratory, where they were unfed and acclimated for 3 days (14 °C, darkness, aerated La Nied water).

Toxicity assay. The assay was designed to evaluate the effects of mask ageing on *Gammarus roeselii* survival and growth. Four food resources were tested: Leaf litter used as control food (alder, *Aulnus Glutinosa; L,* cf. §2.3)*,* pristine masks and 1d or 3d photodegraded masks immersed in the Moselle River for 4 weeks. Each condition was replicated 18 times. Each microcosm consisted of a 60 mL glass tank containing 30 mL of La Nied-filtered (GF/F Whatman filter, nominal cut off 0.7µm) stream water, one *G. roeselii,* and two 8 mm diameter-discs of chosen food resource. The reader is referred to **Appendix A** for details on the conditioning of food resource disks and on the *G. roeselii* organisms. The assay was conducted for 14 days in a temperature-controlled chamber (14±1°C) under dark condition. Gammarids were allowed to feed *ad libitum.* To limit chemical variations, La Nied River water in each tank and resources were renewed every week. For each replicate, water and discs remaining prior to resource renewal were frozen at -20 °C for assessment of plastic fibre dispersion and feeding rate, respectively.

Endpoints. The number of dead gammarids was recorded daily: death date was recorded and dead gammarids were removed. After 14 days exposure, gammarid individuals were rapidly photographed for size assessment (see above; (final - initial size)/(initial size x time); in $days^{-1}$), transferred in 1.5 mL Eppendorf tubes containing 1 mL of ethanol at 70% and finally stored at 4°C until gut content analysis.

Gut content analysis. Diet composition of (living) *G. roeselii* at the end of the experiment was determined by gut content analyses according to Felten et al. (2008). Briefly, dissected foregut contents were placed into a drop of water on microscope slides, homogenized, then examined at different magnifications from x40 to x400 (Epifluorescence microscope Olympus BX41) to assess the approximate percentage (by area) of seven recorded items: (i) animal material, (ii) FPOM (fine particulate organic matter corresponding to amorphous detritus lacking well-defined cellular structure), (iii) diatoms, (iv) filamentous algae, (v) CPOM (coarse particulate organic matter: mainly leaf detritus with brownish palisade cell layers), (vi) small mineral particles, and (vii) plastic fibers.

Fibres in gut and water analysis. Plastic fibres were visually counted using Olympus BX41 microscope and sized using the VHX-6000_950F associated software (Keyence Corporation).

Statistical analysis. Time-to-event data analysis was used to investigate the direct or indirect (i.e. mask as a support of food resource) effects of mask and its ageing on *G. roeselii* survival. This approach allowed to (i) consider events occurring during the whole study period (not only at the final time point) and (ii) account for right-censored values, i.e. organisms whose death was not observed within the study period. Kaplan-Meier curves were used for time-to-event data representation. Log-rank tests were performed to compare survival curves between pairwise treatments. Bonferroni correction was applied for multiple comparisons (n=3 ad hoc planned pairwise comparisons). To test differences between treatments, one-way ANOVAs were performed when assumptions concerning normality of data distribution (Shapiro-Wilk test) and homoscedasticity (Bartlett test) were met, followed by post-hoc Tukey tests. When ANOVA assumptions were not met, Kruskall-Wallis tests were used followed by Mann Whitney test with Bonferroni correction for pairwise comparisons. Data analyses were implemented in R statistical environment (R Core Team, 2019). A significant level of $p \leq 0.05$ was considered.

3. Results and discussion

The first step of our work consisted in exposing masks to UV-radiation. After 28 days exposure, the 3 different mask layers (IL, OL and ML) were completely shredded (**Appendix C**, **Figure C.1**) and their manipulation was impaired by their easy disintegration into powder. Despite of this difficulty, it was possible to separate properly the different layers with tweezers. For masks subjected to shorter UV exposure, degradation was less pronounced even though signs of alteration were clearly visible by eyes after 3 days exposure with the appearance of tears at the folding zones of the intermediate layer. We further observed that ML, IL and OL became brittle after 24, 48 and 72 hours of UV exposure, respectively.

3.1. Bulk material characterization of pristine and photodegraded mask layers.

Elemental compositions of pristine mask layers are reported in **Figure 1A.** Overall, the chemical composition reflects the nature of the inorganic additives used as pigments in masks or employed as fillers to reduce costs and improve mechanical properties. In particular, the identified elements Na, Mg, Al, Si, P, S, K and Ca probably originate from mineral phases like talc, mica, kaolinite, calcium and magnesium carbonate or barium sulphate, all commonly added to reinforce polymers (Ren et al., 2002; Shrivastava, 2018). The analysis further reveals the presence of Ti, Zn, S and Ba that enter the composition of white pigments like titanium oxide or lithopone (co-precipitate of zinc sulphide and barium), the former being the most frequently adopted pigment (Al-Malaika et al., 2017). Differences in composition are observed depending on the layer type considered. Indeed, the amount of titanium is lowest in ML, barium is mainly detected in IL and the only OL contains copper. The presence of copper may be connected to the blue colour of OL since this metal is one of the components of the blue pigment copper phtalocyanine (Gooch, 2002).

X-ray diffractograms are shown in **Figures 1B(a)-(c)**. Regardless of UV exposure, Bragg's reflections pertaining to OL and IL (**Figures 1B(a),(c)**, respectively) reveal the presence of the α-monoclinic phase of polypropylene (PP) (Machado et al., 2005) with an additional halo corresponding to the amorphous phase. Values of the crystallinity index CI_X obtained from diffraction data are reported in **Table 1** for IL, OL and ML depending on UV exposure duration. For IL and OL, CI_X ranges from 0.42 to 0.78, in

434 agreement with 0.5 value given by Machado et al. (2005) and Kotek et al. (2004), and with the 0.5-0.77
435 range in Isasi et al. (1999). In addition, there is no obvious correlation between Cl_X and ageing time.

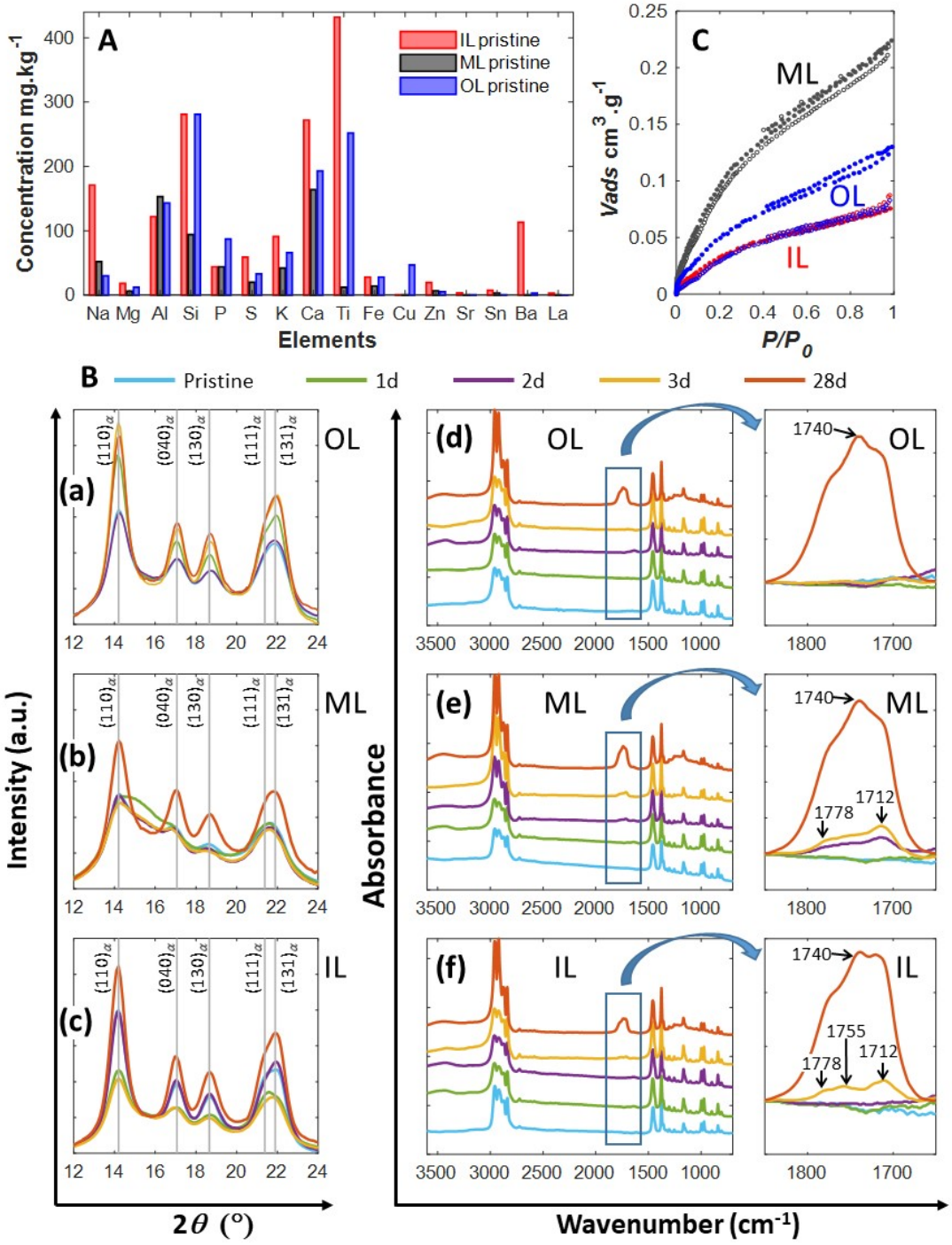

Figure 1. (A) Elemental chemical composition determined by ICP-MS for the three different layers prior to exposure (pristine). IL: inner layer, ML: middle layer, OL: outer layer (indicated). Only elements with concentrations larger than 3 mg/kg are reported for the sake of clarity. **(B)** panels **(a)-(c)**: Wide Angle X-ray Scattering (WAXS) curves expressed in intensity versus diffraction angle 2θ (in degrees), recorded with Cu Kα microsource. OL: outer layer **(a)**, ML: middle layer **(b)**, IL: inner layer **(c)**. **(B)** panels **(d)-(f)**: Fourier Transform Infrared spectra (FTIR) recorded in transmission mode and expressed as a function of the wavenumber, with a zoom on the spectral region corresponding to carbonyl groups (right column). OL: outer layer **(d)**, ML: middle layer **(e)** and IL: inner layer **(f)**. In **(B)** panels **(a) to (f)**, Pristine: no exposure; 1d, 2d, 3d, 28d: samples after 1 day, 2 days, 3 days and 28 days UV-exposure, respectively. **(C)** Krypton adsorption isotherms collected on OL, ML and IL

(indicated), before UV-exposure (pristine, open circles) and after 28 days under UV radiation (full circles). The volume of adsorbed gas is plotted as a function of the relative pressure P/P_0.

436

437 **Table 1.** Parameters derived from material characterization methods. CI_X: crystallinity index calculated
438 from WAXS. HC_{IR}: helical content derived from FTIR spectra. CaI_{IR}: carbonyl index estimated from FTIR
439 spectra. R_a and R_q: roughness parameters obtained from AFM maps representing surface height
440 variations, with R_a and R_q the arithmetic average and root mean square of these deviations,
441 respectively. Results derived from krypton adsorption experiments: SSA (specific surface area), C
442 (surface energy constant) and E_1 (enthalpy of adsorption for the first gas layer). OL, ML, IL: outer,
443 middle and inner layer, respectively. p: pristine (no UV exposure). 1d-28d: duration of UV-exposure in
444 days. For the inner pristine layer, R_a and R_q were calculated on the basis of a single image.

	CI_X (no unit)	HC_{IR} (no unit)	CaI_{IR} (no unit)	AFM		Kr adsorption		
				R_a (nm)	R_q (nm)	SSA ($m^2\ g^{-1}$)	C constant (no unit)	E_1 ($J\ mol^{-1}$)
OLp	0.50	0.84	0.20	4.4±1.5	5.9±2.3	0.26	4.07	9979
OL1d	0.67	0.88	0.21					
OL2d	0.48	0.88	0.16					
OL3d	0.78	0.95	0.16					
OL28d	0.70	0.93	1.48	4.9±3.2	6.6±4.6	0.30	10.92	10610
MLp	0.27	0.85	0.24	4.8±1.4	6.0±1.5	0.60	7.67	10384
ML1d	0.17	0.88	0.16					
ML2d	0.29	0.95	0.33					
ML3d	0.24	0.90	0.40					
ML28d	0.72	0.88	1.83	4.8±2.0	6.2±2.5	0.60	9.94	10550
ILp	0.69	0.90	0.15	3.2	4.4	0.25	4.60	10057
IL1d	0.42	0.88	0.18					
IL2d	0.70	0.89	0.19					
IL3d	0.42	0.85	0.28					
IL28d	0.74	0.92	1.21	4.2±0.8	5.4±1.1	0.21	8.96	10484

445

446 The dispersion of CI_X values may be attributed to intrinsic spatial heterogeneities of mask samples.
447 Indeed, the size of X-ray beam (diameter<300 µm) did not make it possible to analyse a volume
448 representative of the whole sample where heterogeneities effects would be averaged. This dispersion
449 of CI_X-data between samples is further consistent with results by Celina et al. (1993) who evidenced
450 that oxidation kinetics of PP powder could differ from one particle to another due to differentiated
451 presence of catalytic residues or impurities. Then, constitutive differences in composition of mask
452 specimen likely overrule the effects of oxidation treatment on CI_X value, effects that are probably very
453 limited or absent as judged from data by Kotek et al. (2004) and Aslanzadeh and Haghighat Kish (2010),
454 respectively.

455

456 WAXS curves for ML (**Figure 1B(b)**) differ from those for IL and OL, except after 28 days degradation
457 time. Peaks assigned to ML α-monoclinic phase are barely discernible for all samples except 28 days
458 exposed ones: they all take the form of weak intensity modulations of the amorphous halo. The shape
459 of the signals obtained on ML under such conditions typically correspond to that expected for the
460 mesophase, which is a conformationally disordered phase closely related to the α-monoclinic form
461 (Androsch et al., 2010; Natta and Corradini, 1960; Nishida et al., 2012). The structure of the mesophase
462 is intermediate between that for amorphous and crystalline state: it is characterized by two broad

peaks at 2θ-angles of 15 and 21.6°, which corresponds to 5.9 nm and 4.1 nm distances, respectively (Androsch et al., 2010). For all samples except the one after 28 days degradation, it is necessary to consider 2 split Gaussian functions to fit signal contributions from both mesophase and amorphous component (**Appendix D, Figure D.1**). In turn, crystallinity index CI_X does not fully reflect the crystallinity level of the samples as contributions from mesophase and amorphous phase cannot be differentiated. With this limitation in mind, CI_X was estimated for 0 to 3 days-exposed ML layers in the same way as it was for IL and OL samples, with resulting values that are significantly lower than those for IL and OL and with a relative variability of CI_X from one sample to another.

After 28 days UV exposure, the ML mesophase identified at shorter degradation times disappear (**Figure 1B(b)**) and leaves place to the monoclinic α-phase with a resulting 0.72 crystallinity index, which basically corresponds to maximal values estimated for IL and OL. As a support of this finding, Androsh et al. (2010) evidenced that transformation of mesophase into α-monoclinic structure is triggered by temperature. Interestingly, while these authors showed the mesophase/α-state transition above 60°C with ramp-experiments, the phase transition for our samples does not depend on temperature (despite of alternated irradiating cycles between 50°C and 60°C, taken similar for all samples) but on irradiation duration. This indicates that the phase transition in our case is probably ruled by both thermodynamics and kinetics, and impacted over time by material damages.

To address possible changes of the chemical groups carried by IL, ML and OL samples depending on degradation time, we measured the corresponding FTIR spectra (**Figures 1B(d)-(f)**). The wavenumber domain from 3030 to 2760 cm^{-1} corresponds to stretching vibrations of methyl and methylene groups, and associated bands are clearly saturated in most of investigated IL, ML and OL samples. It is only for sufficiently degraded samples that these bands start to be well resolved, with joint apparition of additional contributions from oxygen-containing products detected in the carbonyl domain (1850 to 1650 cm^{-1}, cf. zooms in **Figures 1B(d)-(f)**) corresponding to >C=O groups (carboxylic acids, esters and ketones, etc) (Lacoste et al., 1993; Luongo, 1960; Philippart et al., 1999). In the range 3600 to 3200 cm^{-1}, the band corresponding to –OH groups (alcohol, hydroperoxides, acids, etc) increases with degradation time, especially so at 28 days UV exposure. In addition, for 28 days-degraded IL, ML and OL specimen, the curves feature a shallow bump in the 1400-1000 cm^{-1} range, which we attribute to C-O-X species (Lacoste et al., 1993).

Using FTIR data, the helical content HC_{IR} was calculated as detailed in Materials and Method section. Values are reported in **Table 1** and vary between 0.84 and 0.95, without clear dependence on the duration of degradation. A stronger impact of UV exposure on HC_{IR} might have been expected after inspection of data by Aslanzadeh and Haghighat Kish (2010) who reported helical content value as high as 0.95 for melt-spun PP fibres after 200 hours ageing at 25°C under UV-C radiation exposure. On the other hand, using attenuated total reflection (ATR) technique, Blais and co-workers (Blais et al., 1972) evidenced a restructuration of the surface layer of PP samples with a continuous increase of the helical content from 0.83 to 1 within UV-A exposure duration as short as 80 h. This effect was however restricted to the outermost surface of their 22 µm-thick samples, as evidenced by measurements in transmission mode that pinpointed the absence of variation of bulk material properties with changing radiation duration. The latter result agrees with our conclusions obtained from FTIR data also collected in transmission mode.

Beside the evaluation of the amount of helical structure at given radiation duration, FTIR unveils useful information on the formation of degradation products over time. In the carbonyl domain (cf. zooms in **Figures 1B(d)-(f)**), a broad ill-defined band can be observed after a delay corresponding to a so-called induction time (Aslanzadeh and Haghighat Kish, 2010; Philippart et al., 1997; Rouillon et al., 2016; Severini et al., 1988). This induction period depends on the layer type considered: 2 days for ML, 3 days for IL and >3 days for OL. The carbonyl index (CaI_{IR}) was computed from the area under the carbonyl band following the procedure given by Almond et al. (2020), and values are summarized in **Table 1**. For radiation durations shorter than the induction period, CaI_{IR} is in the range 0.15 to 0.24, in agreement with the 0.18 value by Almond et al. for pristine PP samples. Maxima of CaI_{IR} are reached at 28 days-degradation time (1.21, 1.83 and 1.48 for IL, ML and OL, respectively) but remain lower than those by Almond et al. (2020) (CaI_{IR}>2 after 20 days irradiation) probably because sample irradiation protocol adopted by these authors is different from ours.

A detailed examination of the carbonyl band (**Figures 1B(d)-(f)**) shows that its shape evolves with UV exposure duration. For the shortest ageing time (IL3d, ML2d and ML3d), the band is broad with a shallow maximum at 1712 cm^{-1} assigned to carboxylic acid in dimer form, and with a shoulder at 1778 cm^{-1} stemming from γ-lactone and/or esters (Lacoste et al., 1993; Philippart et al., 1999). Another shoulder can be distinguished on IL3d at 1755 cm^{-1}, corresponding to free carboxylic acid (Philippart et al., 1999). After 28 days exposure, the main component of the carbonyl band at 1740 cm^{-1} is attributed to esters (Lacoste et al., 1993; Philippart et al., 1999), with the shoulders at 1712 and 1778 cm^{-1} invoked above. This evolution of the carbonyl band with a shift of the maximum of absorption upon increasing exposure duration is well documented in literature (Aslanzadeh and Haghighat Kish, 2010; Rouillon et al., 2016). It is explained by the fact that acetic acid, a molecule of low weight, can migrate from the polymer to the gas phase, unlike macromolecular photoproducts e.g. ester groups and acids that keep on accumulating in the material during degradation (Rouillon et al., 2016).

3.2. Surface properties of pristine and photodegraded mask layers.

As evidenced by SEM (**Figures 2A,B**), the two pristine peripheral layers of the mask (IL and OL) display similar organization, typical of that characterizing thermal bonded non-woven fabrics. Both types of layer consist of a web of fibres with 20 µm average diameter, and the material structure is reinforced with square-shaped bond points clearly observable in the micrographs. The size of the bond differs between IL and OL, with ca. 500 µm and 700 µm dimensions, respectively, and this difference may contribute to differences in IL and OL mechanical properties. Back scattered electrons (BSE) pictures further reveal the presence of round-shaped grains with size lower than 500 nm on the surface of all fibres (**Appendix E, Figure E.1(a)-(b)**). Energy Dispersive X-ray Spectroscopy (EDS) shows that most brilliant grains are composed of titanium and oxygen (**Figure E.1(c)**), which explains their bright appearance on BSE micrographs. In line with this finding, titanium dioxide particles have already been identified on the surface of plastic debris extracted from sediments (Fries et al., 2013). The observation of particles consisting of titanium further agrees with the chemical analysis in **Figure 1A**. The remaining surface of the fragments has a composition reminiscent of minerals with aluminium and silicon elements (**Figure E.1(d)**), it features crystallized salts (e.g. Na, Ca, Cl, S) **(Figure E.1(d)**) or consists of only carbon (**Figure E.1(e)**). All these defining properties are common to pristine IL and OL samples.

After 3 days UV exposure, IL and OL fibres fragmented into rods, the length of which vary from a few tens to several hundreds of microns (**Figures 2D-F** and **Figure E.2 in Appendix E)**. There is no splintered elements at the fibre surface and the observed fractures are rather sharp, even though burrs

appear at some places. **Figures 2D,E** make it clear that photodegradation leads to shorter fibers with a fragmentation that proceeds in a section that is perpendicular to the main axis of the fibers, leading to reduction of fiber length. A description of why such a fragmentation follows this pattern would require a refined analysis of the mechanical features of the fibers and their microstructural properties along the two main directions of the fiber geometry. In addition to fibres fragmentation, cavities are formed on IL and OL after UV exposure (**Figure 2F**). The diameter of corresponding voids amounts to a few hundreds of nanometres and some of them are filled with titanium dioxide nanoparticles (cf. zoom in **Figure 2F**)), thereby suggesting that cavity genesis proceeds according to photocatalytic degradation mediated by TiO_2 (Lee and Li, 2021; Ohtani et al., 1989). Cavities are observed on both fibres surface and sections newly generated by fragmentation (**Figures 2E,F**), therefore implying that titanium particles were located in the core of fibres prior to degradation. After 28 days ageing (**Figures 2G-I** and **Figure E.3 in Appendix E**), rods are still observed and are decorated by multiple micron-sized plastic fragments **(Figure 2G)**. The cavities are still visible on IL and OL fibres, some of them are filled with TiO_2 grains and others not (**Figures E.3(a),(b),(g),(h)**). For both IL and OL, some fibres appear extremely cracked (**Figure 2I**, **Figure E.3(b),(c),(d),(f),(g),(h)**), which confers upon them a laminated and powdery aspect. Some of the observed cracks seem to have grown from the cavities (cf. rectangles in **Figures E.3(b),(h)**). Additional types of defects appear on IL and OL upon ageing, such as surface blister-like structures of a few microns in size (**Figure 2H, Figure E.3(e))**. The main elemental component of these structures is carbon. Overall, we find that fibres are either covered predominantly by the above blister-defects or altered significantly with presence of numerous cracks, and few fibres exhibit both properties (**Figure 2H** and **Figures E.3(d),(f)**). The resulting structural heterogeneity of degraded IL and OL comforts the significant dispersion in CI_X and CaI_{IR} indexes estimated from WAXS and FTIR, respectively.

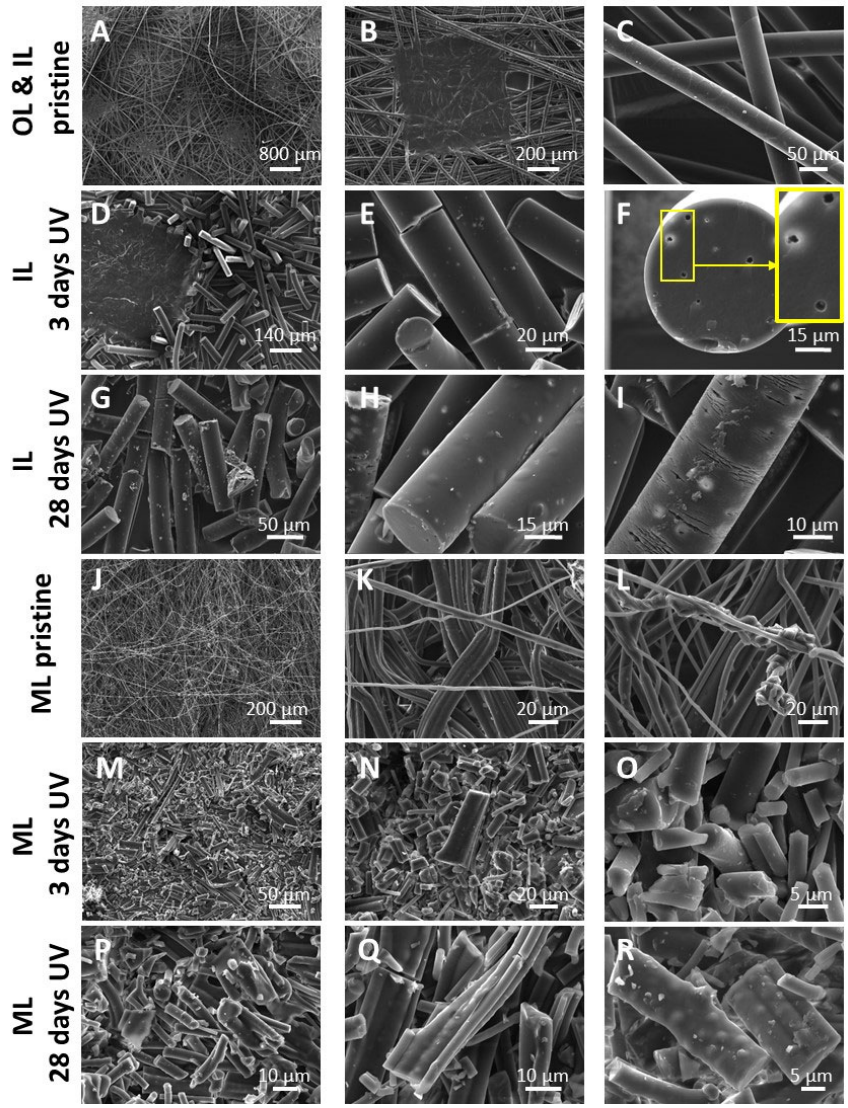

Figure 2. Scanning electron micrographs (secondary electron detection mode). **(A,C)**: pristine inner layer (IL). **(B)**: pristine outer layer (OL). **(D)-(F)**: IL after 3 days UV exposure. **(G)-(I)**: IL after 28 days UV exposure. **(J)-(L)**: pristine middle layer (ML). **(M)-(O)**: ML after 3 days UV exposure. **(P)-(R)**: ML after 28 days UV exposure. Zoom in **(F)** shows that some of the holes are filled with bright nanoparticles, probably TiO_2 according to literature and data of Figure 1A and Figure E.1 in Appendix E.

The structure of pristine ML takes the form of an entangled and heterogeneous network of fibres polydisperse in size (**Figures 2J-L**). In detail, isolated fibres with diameter in the 1.5 to 8 µm range coexist with flat bundles formed from fused fibres, the width of which is ca. 10-20 µm. The few fragments observed on ML fibres are composed of carbon, or they feature a chemical composition typical of salts with the presence of calcium, sodium chloride or sulphate. This finding suggests that these salt entities are not plastic additives but likely originate from exogenous deposits during mask life cycle. Unlike IL and OL, pristine ML are free of TiO_2 nanoparticles. Exposure to UV leads to the formation of elongated fragments, heterogeneous in size and shape **(Figures 2M-O)**. In addition, no cavities nor cracks are observed, irrespectively of the exposure time, while some fragments display blisters after 28 days UV-treatment (**Figures 2P-R**).

As an intermediate conclusion, the above SEM results evidence that UV exposure leads to fragmentation, cracks and cavities formation, and to occurrence of blisters on most degraded samples. To further address the impacts of UV-mediated weathering of samples at the infra-micronic level, we used AFM in contact mode. **Figure F.1** in **Appendix F** reports illustrative AFM images (256×256 pixels) with 5 μm×5 μm dimensions for IL and OL, and 2 μm×2 μm for ML, all recorded on both pristine and 28 days degraded samples. At first sight, there is no change in surface topography with ageing, and all scanned surfaces appear smooth and similar for the 3 fibre types. This qualitative observation is confirmed by values taken by R_a and R_q surface roughness parameters, i.e. 3.2 nm-4.9 nm and 4.4 nm-5.9 nm, respectively (**Table 1**). These data are consistent with those reported elsewhere for different PP forms and radiation procedures (Ma et al., 2021; Rouillon et al., 2016; Slepička et al., 2010).

One drawback of microscopy techniques like SEM and AFM is that observations and related conclusions are based on the analyses of selected objects with possible bias in terms of overall sample representativeness. To circumvent this difficulty, we performed additional surface sample characterization by gas adsorption technique, which has the merit to provide surface properties statistically averaged over the whole sample body. The krypton adsorption isotherms recorded for pristine and 28 days exposed samples are displayed in **Figure 1C** and corresponding BET results are provided in **Table 1**. For all samples, the evaluated specific surface area (SSA) is low (≤0.6 m^2g^{-1}) and does not change noticeably with degradation. As expected, highest surface area is obtained for ML samples that feature the fibers with lowest diameter. Quantitative geometric arguments are provided in **Appendix G** to support the lack of change in SSA with increasing UV exposure and material fragmentation (**Figure G.1** in **Appendix G**, and cf. associated comments). Following these arguments, it is evidenced that the contribution of lateral surfaces in the overall SSA overwhelms that from basal surfaces. In turn, cracks do not contribute much to the overall SSA. The polydispersity of the fibres (in terms of both length and diameter) does not further ease detection of cracks from the only inspection of specific surface area values.

Even if SSA does not change significantly with varying UV-exposure, gas adsorption remains a valuable tool for monitoring effects caused by UV on surfaces. Indeed, BET application to experimental data also allows derivation of the so-called C constant defined by $C = \exp\left[(E_1 - E_l)/R_g T\right]$ which characterizes the interaction between atoms of krypton and surface (Brunauer et al., 1938), with E_1 the enthalpy of adsorption for the first gas layer, E_l is that for subsequent layers and it equates with the enthalpy of liquefaction, R_g is the gas constant and T is the temperature. Values of C are collected in **Table 1** together with E_1 evaluated by considering a Krypton heat of liquefaction of 9.08 kJ/mol. The energy of adsorption of the first layer is found highest for all degraded samples, which reflects a modification of the surface. This difference between initial and end (degraded) state is most pronounced for the two external mask layers (IL and OL). Following arguments by Chow and Grant (1988), difference in the surface energy of pristine and photodegraded PP may result from surface diffusion phenomena mediated by temperature.

3.3. Electrokinetic and stability features of colloidal debris from photodegraded mask layers.

Electrophoretic mobility measurements. **Figure 3A** shows the measured dependence of electrophoretic mobility (μ) of plastic debris suspended in solution *versus* KNO_3 concentration (denoted as c_{KNO3}). These debris originate from photodegraded masks and their constitutive layers once in powdery state. Overall, μ is negative, in line with surface electronegativity of plastic materials (Jacobasch, 1984;

Zimmermann et al., 2001), and magnitude of μ is that of systems that are significantly charged. Remarkably, regardless of sample and UV treatment delay, μ varies with the logarithm of c_{KNO3} according to a characteristic quadratic-like curve (termed hereafter 'banana' profile) with a marked minimum at ca. 10 mM. In addition, μ tends asymptotically toward a non-zero plateau value at sufficiently large c_{KNO3}, as further evidenced by **Figure H.1** (**Appendix H**). This plateau-property is the signature of the electrokinetic behaviour of so called-soft particles, i.e. particles whose 3D surface structure is permeable to electroosmotic flow (Gopmandal and Duval, 2022). Similarly, hard (impermeable) particles featuring a surface roughness comparable to the Debye length can exhibit such an electrokinetic response as particle charges probed by the electroosmotic flow are then effectively distributed within a 3D region (Duval et al., 2004; Škvarla, 2007).

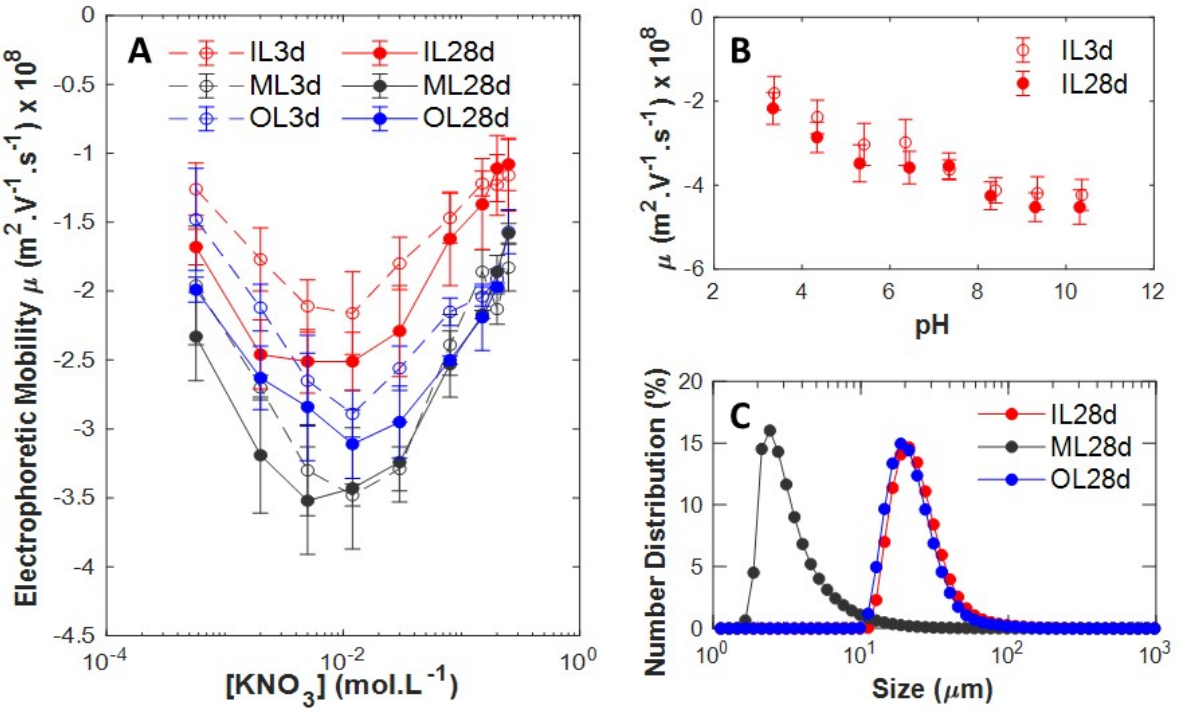

Figure 3. (A) Electrophoretic mobility (μ) measured on masks debris dispersed in KNO_3 electrolyte as a function of KNO_3 concentration at pH 7.35. IL: inner layer, ML: middle layer, OL: outer layer. 3d, 28d: debris after 3 days and 28 days UV-exposure, respectively. Dotted and solid lines: electrophoretic mobility for layers after 3 days and 28 days UV exposure, respectively. Errors bars correspond to triplicate measurements. **(B)** pH-dependence of the electrophoretic mobility of fragments of the inner layer after 3 days (IL3d) and 28 days (IL28d) UV-exposure. Measurements were performed in 1.2×10^{-2} mol/L KNO_3 electrolyte. (**C)** Size distributions measured by laser diffraction on 28 days UV-aged debris dispersed in water. The distributions are expressed in number percentage. IL: inner layer, ML: middle layer, OL: outer layer.

Obviously, the plastic debris of interest here are representatives of this second type of particles, recalling that the Debye length varies between ca. 10 nm and 1 nm with increasing salt concentration from 1 to 100 mM, to be compared with the obtained surface roughness R_a~3.2-4.9 nm (**Table 1**). The decrease of μ (in absolute value) with increasing c_{KNO3} above ca. 10 mM is a consequence of the increased screening of debris surface charge by ions from background electrolyte. The decrease of μ (in absolute value) with decreasing electrolyte concentration below 10 mM can originate from several processes already documented in literature for different particulate materials. In detail, Duval et al. (2013) reported such a non-monotonous electrophoretic behaviour for highly charged latex

nanoparticles and argued that it is caused by electric double layer polarization, in line with quantitative predictions from soft surface electrokinetic theory. Interestingly, these latex particles exhibited an outer fuzzy surface layer of ca. 1 nm in thickness, which is of the order of magnitude of the surface roughness of our colloidal plastic debris. Given the nature of these debris (cf. SEM pictures in **Figure 2**) and their characteristic surface roughness, it is likely that the minimum in μ is caused by electric double layer polarization effects, similarly to that observed for latex particles.

When comparing the electrophoretic mobility-c_{KNO3} patterns collected for all samples of interest, we observe that the 'banana' profile associated with a given 28 days-degraded layer type is basically shifted towards more negative μ values as compared to that for its 3 days exposure analogue. In addition, regardless of the treatment delay, 'banana' profiles pertaining to colloidal residues from IL, ML and OL are shifted one with respect to the other according to the sequence $|\mu(\text{IL})|<|\mu(\text{OL})|<|\mu(\text{ML})|$. Qualitatively, the positioning of the banana profiles displayed in **Figure 3A** is likely explained by the presence of additives of different nature (**Figure 1A**) depending on layer type considered, by the possible generation of ionisable surface groups following UV treatment (cf. §3.1) and/or by the way in which the particle surface roughness is affected by that treatment. Related to the latter point, whereas AFM measurements (**Figure E.1**) do not evidence significant change in roughness of lateral surface of fibres, it cannot be excluded that an increase in mean particle surface roughness (evidenced by SEM, **Figure 2**) due to newly created basal surfaces (fractured areas) affects the electrophoretic mobility of masks debris.

In **Figure 3B** we report the dependence of μ on pH at c_{KNO3}=12 mM for IL3d and IL28d. Overall, μ increases (in absolute value) with increasing pH from 3 to 5, it levels off from pH 5 to ca. 7-7.5, and it increases with further increasing pH before reaching a plateau value at pH>8. Unlike electrokinetic data on non-degraded PP surfaces measured (mostly) by streaming potential technique (Aranberri-Askargorta et al., 2003; Ismail et al., 2021; Košíková et al., 1995), our measurements do not evidence an isoelectric point in the pH range 3 to 10. They rather indicate that charge of debris originates from two different types of acidic functional groups whose complete dissociations are marked by the two aforementioned plateau regimes in the μ *versus* pH representation. Based on spectroscopic data given in **Figure 1B(d)-(f)**, the deprotonable functional groups revealed by electrokinetics are likely of the forms R-O-OH (e.g. hydroperoxide), R-OH (hydroxide) or R-COOH (carboxylic acid). It is remarkable that the pH-dependence of μ identified in this work significantly deviates from the quasi-linearity expected for hydrophobic polymer materials like PP (Ismail et al., 2021; Slepička et al., 2010), PE or PET (Jacobasch, 1984) (Zimmermann et al., 2001). Accordingly, the samples investigated here most likely exhibit a polar character that can be connected to the polar functional groups revealed by FTIR. Even if these groups surely determine the hydrophilic properties of aged samples, the presence of hydrophobic patches cannot be ruled out, as evidenced by Song et al. for UV-irradiated poly(dimethylsiloxane) surfaces (Song et al., 2007). The overall hydrophobicity/hydrophilicity balance of the colloidal mask fragments goes in the sense of a gain in hydrophilicity with increasing UV-exposure as evidenced by electrokinetics *and* by the difficulty to properly disperse the fragments released by 1-day UV-exposed masks. This conclusion agrees with the results by Alimi et al. (2023) on the reduced sorption capacity of weathered microplastics to hydrophobic contaminants (triclosan). Last, the nature of the adopted degradation treatment seems to be of outmost importance in defining the electrostatic features of the surfaces, including sign of the charge. Indeed, whereas (Slepička et al., 2010) reported an increase in μ towards positive values for PP surfaces subjected to argon-plasma irradiation, our results display an opposite trend for PP materials exposed to UV for 3 and 28 days (**Figure 3A**). Moreover, results provided in **Figure 3B** *versus* pH do not show significant change in debris

charge with increasing UV-exposure duration, which agrees with the similar slopes μ *versus* log(c_{KNO3}) at c_{KNO3} > 100 mM in **Figure 3A**.

Granulometry. Granulometry results are given in **Figure 3C** for samples exposed to UV for 28 days. Data acquired on 3 days UV-exposed samples were not considered for such measurements, as they were not reproducible. The reason originates from the fact that 3 days-aged samples exhibited a more pronounced hydrophobic character than 28 days exposed samples. Accordingly, they tended to stick on vessel surfaces, and the granulometry stirring conditions further favoured the trapping of air bubbles with plastic fragments. For all 3 samples tested, the size distributions are asymmetric and present a mode that roughly corresponds to fibre diameters (2.4 µm, 18.7 µm and 21.2 µm for ML, OL and IL, respectively). Small fragments possibly originating from the fibre fracture zones were possibly present but they could not be detected due to their weak contribution compared to that of larger debris. Interestingly, size distribution of ML sample is shifted significantly to lower sizes as compared to the other two layer types. In contrast, the electrophoretic mobility collected for the three layers did not differ much within experimental error, therefore suggesting that the electrophoretic response of the layer debris is dominated by local modifications of layer structure - as argued in the preceding section - rather than by changes in debris size. This absence of dependence of electrophoretic mobility on particle size is in line with the fact that the particles dimensions well exceed the Debye layer thickness and, therefore, that retardation effects and electric double layer polarization are not significant (Duval and Ohshima, 2006).

3.4. Effects of UV-treatment on the physicochemical properties of masks and their colloidal debris: summary.

The experimental data detailed in the previous sections make it possible to sketch an overview of the impacts of photodegradation on the physicochemical properties of surgical face masks (**Figure 4**) and their released debris in aquatic media. Although results were obtained here for a specific brand of mask under artificial ageing conditions, they may be considered generic as literature evidences similar fibre release irrespectively of mask brands (Wu et al., 2022) or similar spectral signature of degradation for masks either aged artificially or collected on beaches (Saliu et al., 2021). Each horizontal bar in **Figure 4** summarizes qualitatively the measured evolution of a given material property as a function of UV-exposure delay, with the following colour nomenclature: white for unavailable data, blue for a property that has not significantly changed, orange for one that has significantly evolved. It should be pointed out that it was not possible to perform electrophoretic mobility measurements on pristine masks. Indeed, even after cutting them into small pieces, it was impossible to prepare a proper colloidal suspension of mask fragments as the latter were floating at the surface of the electrolyte mainly because of their hydrophobic property.

The first striking feature revealed by **Figure 4** is that changes of macroscopic mask properties inferred from sample manipulation systematically occur before bulk material properties start to evolve significantly. Indeed, after three days of UV-exposure, the material becomes brittle and breaks up easily. It then became less difficult to disperse it in water, therefore suggesting that neo-formed fragments are less hydrophobic. Concerning PP bulk properties evaluated by WAXS, the main modification is the change after 28 days of the crystal structure of ML from a conformationally disordered phase (mesophase) to the α-monoclinic structure, with a companion increase in crystallinity. This crystal transformation is the only change of material property revealed by X-rays scattering analysis. Crystallinity for IL and OL varies from one sample to another, with no obvious

dependence on UV exposure time. The same conclusion holds for the helical content index evaluated for IL, OL and ML by FTIR. The quantity of chains in helicoidal conformation, as reflected by this index, does not depend on the duration of degradation. In addition, the helical content is surprisingly of the same order of magnitude for both mesophase and α-monoclinic phase. Among all parameters that define bulk plastic materials, it is the carbonyl index that most clearly changes with duration of photodegradation. Significant changes of this index are identified only for conditions marking extreme variations in macroscopic material properties. This finding is in agreement with literature results that report a period of induction for the increase in the carbonyl band (Benítez et al., 2013; Philippart et al., 1997; Rouillon et al., 2016; Severini et al., 1988). The loss of mechanical properties and the emission of organic molecules (cf. below) could be detected prior to increase of the carbonyl index (Aslanzadeh and Haghighat Kish, 2010; Rouillon et al., 2016). UV action leads to fragmentation of fibers into rods, which proceeds by the generation of transverse fractures (Aslanzadeh and Haghighat Kish, 2010; Kotek et al., 2004). There is no variation of the surface roughness of fibers that are further devoid of flakes or peels. Instead, the surface of fibers only features craters, some of them formed around titanium dioxide particles, which likely results from the photocatalytic properties of this mineral. Even though most fragments produced by degradation have rod shape with a few tens of microns length, there is also generation of submicronic particles deposited at the rods surface, as observed by SEM.

As shown in **Figures 3A,B** the electrophoretic properties of mask fragments feature particles with significant electrostatic charge, and these properties are not characteristic of those expected for non-polar materials. They further depend moderately on UV exposure duration and layer type. All electrokinetic data follow a characteristic 'banana curve' marking the dependence of electrophoretic mobility on salt concentration. Remarkably, this 'banana curve' is also measured for PP granulates exposed to UV lamp (cf. details in **Appendix I** and **Figure I.1** therein), even though mask fragments are 2 to 3 orders of magnitude larger in size (**Figure I.2** in **Appendix I** and **Figure 3C**). This supports the idea that the surface reactivity of plastic debris is not dominated by size.

As a last remark, SEM and EDS results reveal that the degradation of mask materials favours the surface exposure (and possible release) of contaminants like TiO_2 nanoparticles which are otherwise embedded in the bulk material, and these contaminants are further found at the surface of the fibres after fragmentation. Obviously, this change in the location of TiO_2 nanoparticles may have important implications in terms of ecotoxicological risk. As far as organic moieties are concerned, we measured an overall release of acetate, citrate, formate and lactate from UV-exposed mask layers over a period of 3 months with a slight increase of the released amount with increasing UV exposure duration, especially so after 7 days monitoring (**Figure J.1** in **Appendix J**). Finally, we suggest that photodegradation leads to the migration of some molecular compounds from bulk to surface, as suggested by CSLM measurements that pinpoint a displacement of auto-fluorescent species with increasing UV-mediated ageing of the materials (**Figure 5**). The fluorescence of UV-aged samples (**Figures 5A(b),B(b),C(b)**) appears in the form of well-defined spots located on the surface of the fibres, whereas that of pristine samples is distributed in the bulk of the fibres according to a pebbled pattern (**Figures 5A(a),B(a),C(a)**). Regardless of the layer type, the blisters observed by SEM on fibres surface (**Figures 5A(c),B(c),C(c)**) concentrate the fluorescence imaged by CSLM, which supports the idea of an ageing-mediated diffusion of organics.

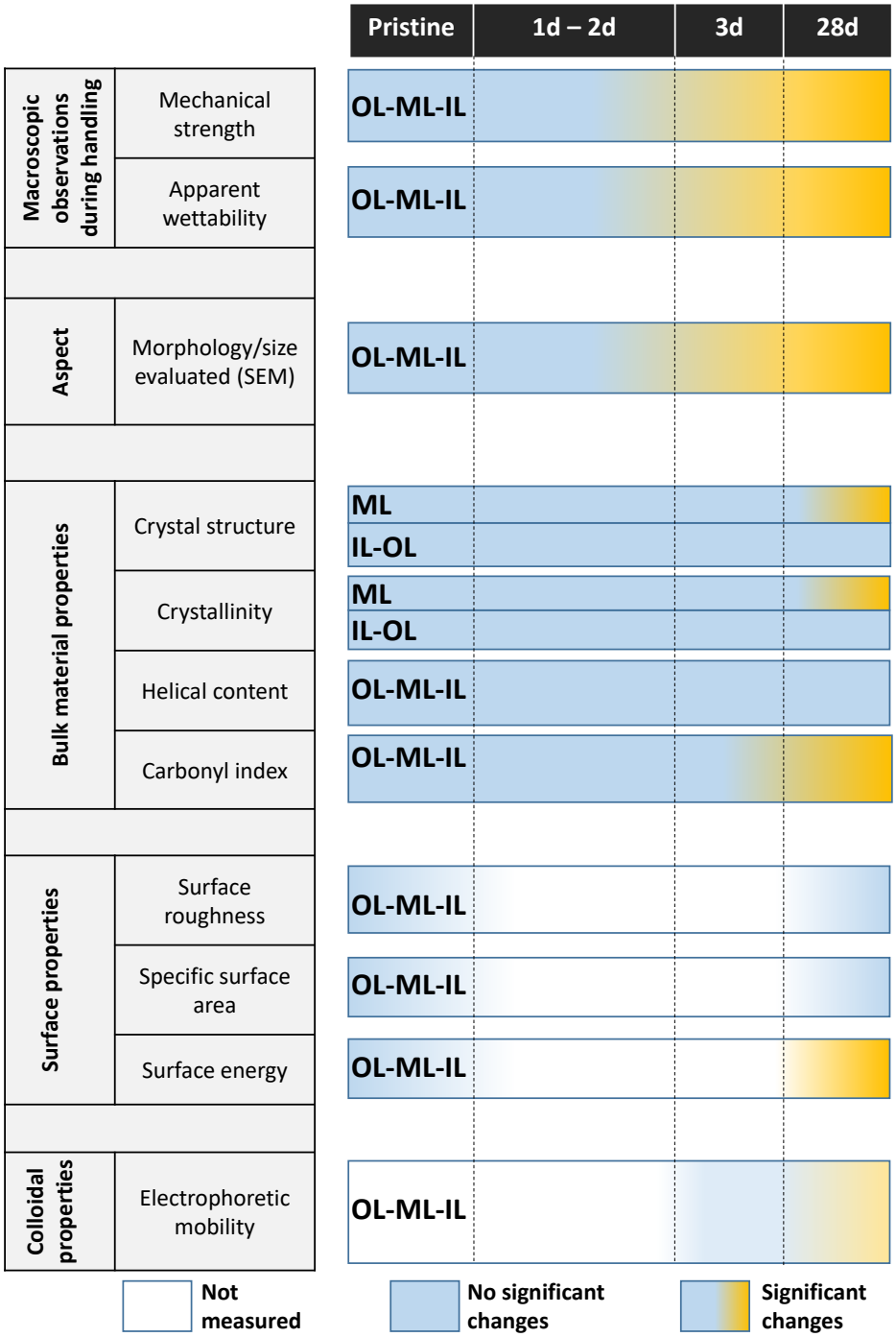

Figure 4. Scheme illustrating the evolution of material physicochemical properties (indicated) as a function of UV-exposure, relative to the pristine initial state. The colour blue means that properties do not change significantly, transition from blue to orange indicates major changes and white colour indicates that the property is not measured. The type of layer concerned with the depicted evolution is specified.

788

789

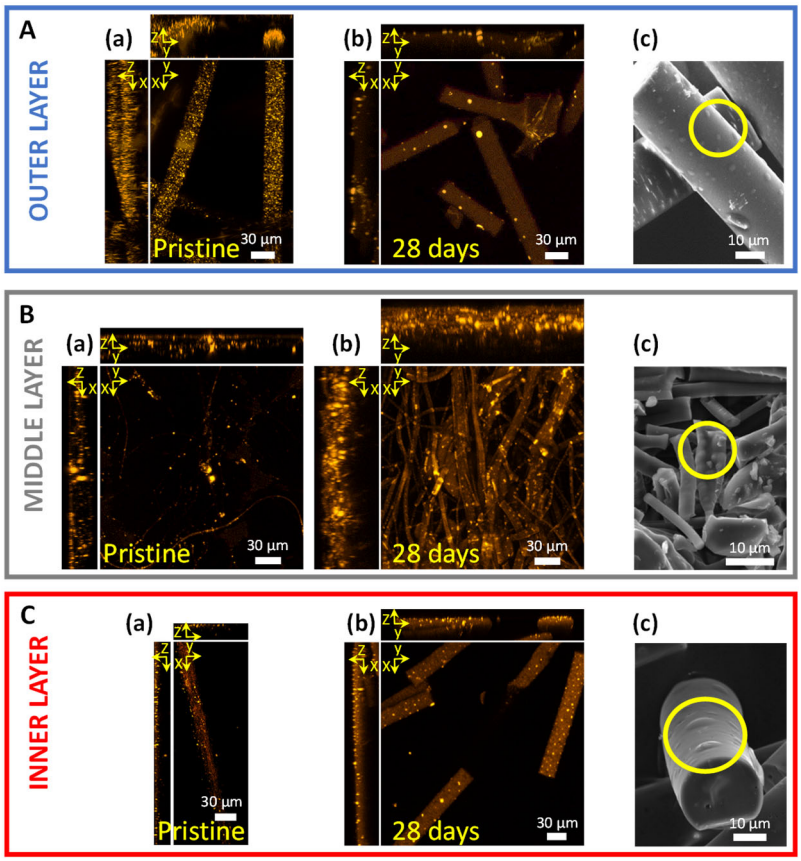

Figure 5. Orthogonal views of the Maximum Intensity Projections (MIP) derived from z-stacks by Confocal Laser Scanning Microscopy (CLSM) for OL **(A)**, ML **(B)** and IL **(C)** in pristine state **(a)** and after 28 days UV-exposure **(b)**. The results evidence changes in the fluorescence distribution due to photodegradation: the fluorescence of UV-aged samples is mainly located on the surface of the fibres whereas that of pristine samples is distributed in the bulk of the fibres according to a pebbled pattern. **(c)** SEM micrographs recorded on 28 days UV-exposed fragments (back scattered electron detection). Yellow circles highlight the blisters displaying fluorescence.

Following the multiscale physicochemical characterization of masks summarized in **Figure 4**, a question remains: do the observed modifications of masks following photodegradation impact on their reactivity towards aquatic biota? This issue is tackled in developments below where we analysed (i) the extent by which photodegradation of masks (prior to their 4 weeks-immersion in Moselle River) alters the composition of subsequently formed freshwater biofilms, and (ii) the mortality of *Gammarus roeselii* species fed in the laboratory with the biofilms grown on the masks.

3.5. Photodegradation of masks: implications for their reactivity towards aquatic biota.

3.5.1. Characterization of river-biofilm formed on masks.

After 4 weeks incubation in Moselle River, pristine and 1 or 3 days UV-exposed mask samples were collected and brought back to the laboratory. DNA quantities obtained on 1-cm diameter discs are given in **Figure 6A.** With increasing the level of UV-mediated alteration, the data reveal a well-marked decrease of the mean total DNA concentration extracted from the masks and therewith a reduction of the overall biomass in the biofilms. However, this conclusion is tempered by ANOVA test that suggests a non-statistical significance of the observed trend ($p=0.113$). In addition, for the same amount of extracted DNA analysed, the number of 16S rRNA gene copies seems to be lower on photodegraded

masks, thus indicating a reduction in the number of bacteria within the biofilms (**Figure 6B**). Here again these differences are poorly marked according to ANOVA test (p=0.0885). Bacteria and algae (mainly diatoms) are found to be the main components of the biofilms formed on masks (**Figure 6C**). This finding is commonly reported for the type of environment considered here (Cooksey and Wigglesworth-Cooksey, 1995) as diatoms and bacteria are considered as pioneering species for the development of photic biofilms (Rao et al., 1997), and they act as the major primary producers and consumers of organic matter, respectively.

The ratio between bacteria and algae (mainly diatoms) is significantly affected by the level of photodegradation (**Figure 6C**; ANOVA; p=0.0369), while the structure of the bacterial community remains almost unchanged (**Figure 6D and Figure K.1 in Appendix K**). Diversity of bacteria on these artificial supports is relatively large with 7 bacterial classes represented (> 1% of the total sequences recovered). The most dominant phyla are *Proteobacteria*, *Bacteroidetes*, *Verrucomicrobia*, *Planctomycetes*, and to a lower extent, *Acidobacteria*, *Cyanobacteria* and *Armatimonadetes* (**Figure K.1(a)**). At a class-distribution level, 12 bacterial classes are identified, the most dominant being the *Gamma-* and *Beta-proteobacteria* (**Figure K.1(b)**). Regarding microalgae, small pennate diatoms (10-11 µm) like *Achnanthidium* dominate the communities (**Table L.1** in **Appendix L**). Diatoms belonging to the *Encyonema* and *Amphora* genera are also well represented, especially on altered masks. Whereas masks were exposed under similar sunlight conditions in the river, we observe a strong heterogeneity within biofilm planktonic communities with sometimes a high relative abundance of Chlorophytes belonging to the *Characium* genus, or *Chaetophorales*, *Chlamydomonadales, Ulotrichales* orders (**Table K.1**). Cyanobacteria from the *Synechococcales* order (*Leptolyngbya* and *Heteroleibleinia* genera) are also widely represented in different biofilms we analysed.

CLSM observations confirm the high diversity of microorganisms adsorbed on masks and further reveal that biofilm structure is mainly dominated by the spatial organization of the constitutive mask fibres as microorganisms are preferentially located in their vicinity (**Figures 6E and 6F**). Additional CLSM images displayed in **Figure M.1** (**Appendix M**) illustrate the variety of solitary (e.g. **Figures M.1(a)-(e)**) or in-groups (filaments or colonies, **Figures M.1(f)-(i)**) freshwater algae found on masks. Some of these colonies also wrap the mask fibres (**Appendix M, Figures M.1(g),(h),(i)**). However, no obvious relationship could be inferred between the degree of degradation of the UV-exposed PP fibres and such occurrences. Most of the fluorescence from phytoplankton organisms is recorded in the red channel (e.g. **Figures M.1(a),(f)**)), corresponding to chlorophyll emission (> 641 nm), and for a few cells in both the red and orange (570-632 nm) channels, resulting in white pixels (**Figure M.1(g),(h),(i)**). In that latter case, it is likely that fluorescence recorded in the orange channel is emitted by some blue pigments (e.g. phycobiliprotein) involved in microphytes photosynthesis. Most of the diatoms observed are in motion outside the biofilm and located on the glass bottom of the dish used for microscopy observations (**Figure M.1(a)**). CSLM pictures also show the occurrence of platy particles, a few tens of microns in size, emitting fluorescence in the green channel (channel 1: 499-561 nm). The shape of these objects suggests that they are of mineral composition, as confirmed by electron microscopy observation with EDS analyses and loss on ignition measurements (**Figure N.1** and **Figure N.2** in **Appendix N**). The micrographs evidence that these platy particles are aggregates of submicronic entities consisting of carbonates and aluminosilicates (**Figure N.1**).

To summarize, results show that masks acting as inert supports for microorganism growth (i.e. they are not a source of nutrients) can host high microbial diversity and abundance. CSLM data do not reveal any preferential adhesion locations of microorganisms versus mask photodegradation, which suggests an apparent lack of connection between bioadhesion and UV-mediated changes in physicochemical properties of fibers. However, macroscopic observations (**Figure N.3 in Appendix N**) evidence that it is

the entangled organization of the fibers that acts as an efficient trap for phytoplankton and mineral particles, while locations corresponding to thermal bond points are by far lesser covered by biofilm. Overall, mask ageing primarily reduces the abundance of algae (mainly diatoms), as confirmed by independent *Nitzschia palea* diatoms colonization assays performed in laboratory as a function of mask UV-exposure duration (not shown). This decrease in mask colonization by diatoms with ageing may result from the decrease of mask hydrophobicity (diatoms would be sensitive to) observed for the colloidal fragments. Mask ageing further poorly affects both bacteria abundance and microbial community structure, which pinpoints that bacteria are less sensitive to changes in fibre surface properties (in particular hydrophobicity) than diatoms.

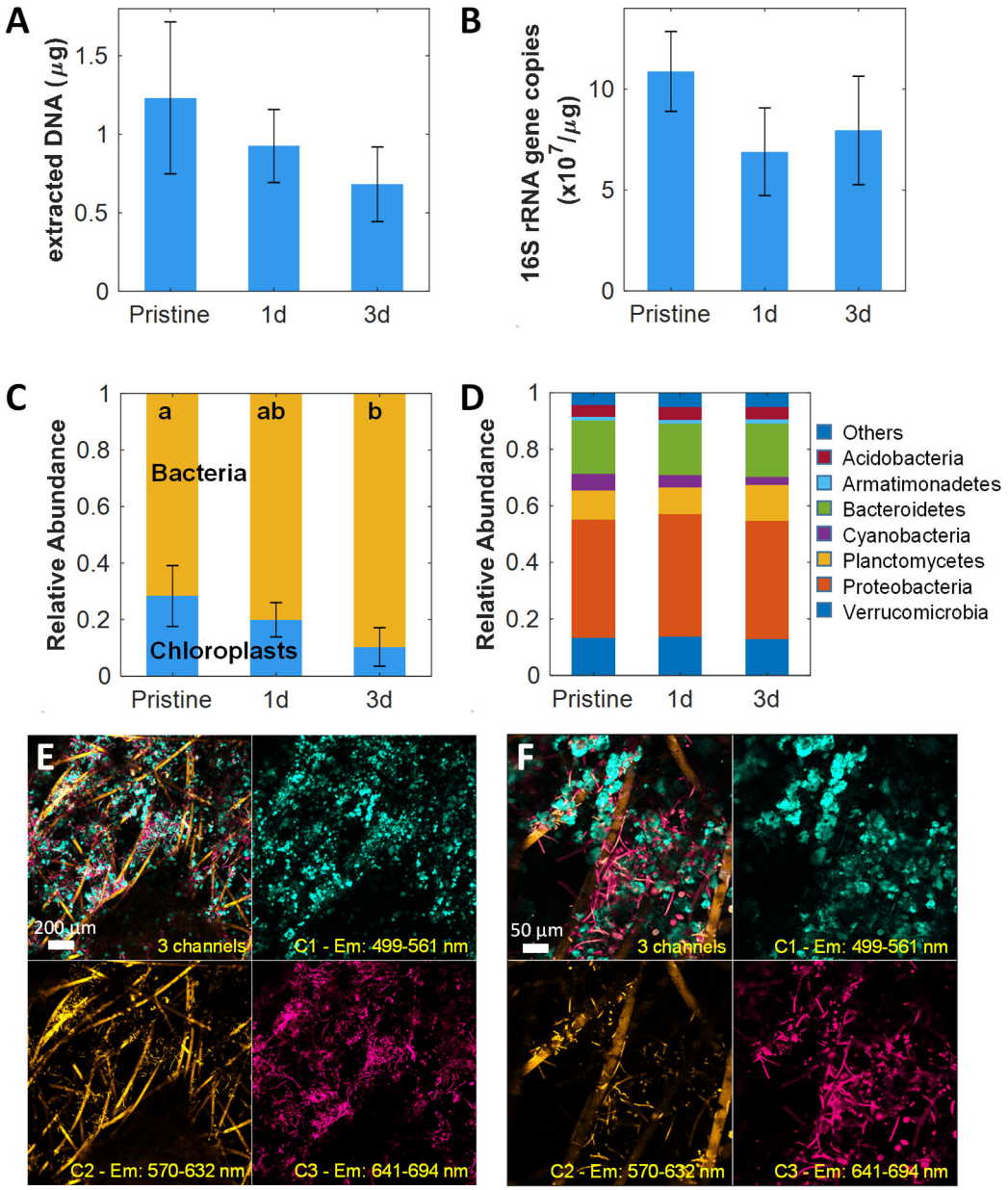

Figure 6. Microbial diversity analysis of biofilms on masks incubated 4 weeks in the Moselle River. Pristine: no exposure; 1d and 3d: masks after 1 day and 3 days of UV-exposure. For each condition, 4 replicates corresponding to 4 different masks were averaged. **(A)** Biomass determined by the total amount of DNA extracted. **(B)** Bacterial abundance, determined by the number of 16S rRNA gene copies. ANOVA p-values are 0.11 and 0.08 in Figure 6A and 6B, respectively. **(C)** Estimation of the bacteria/algae ratio within biofilms based on the ratio of 16S rRNA sequences from bacteria and chloroplasts. Lowercase letters a, ab and b in panel C indicate significant differences

(p<0.05). **(D)** Bacterial community structure analysis at the phylum-level. Others include phyla with < 1% average relative abundance and unaffiliated sequences. **(E)**,**(F)** CLSM images showing the autofluorescence of the components of biofilms on pristine masks after incubation in the Moselle River at two different magnifications. Autofluorescence was recorded over three different spectral ranges (C1, C2, C3) specified in each panel. The colour adopted for each channel corresponds to the median detection wavelength in that channel. In (E) and (F), the upper left tile is the image after merging of the 3 channels.

3.5.2. Ecotoxicity and gut content of G. roeselii.

High survival (ca. 90%) was recorded for gammarids fed on alder litter during 14 days. According to Kaplan-Meyer curves analyses, survival of *G. roeselii* is significantly affected by the type of resource (Log rank test, p=0.005; **Figure 7A**): the survival of gammarids fed on leaf litter is significantly higher than that of organisms fed on mask (leaf *vs* masks: p<0.005), whereas those fed on pristine masks show a significantly higher survival (72%) compared to those fed on aged masks (pristine *vs.* aged masks: Log rank test, p=0.014; 1d: 33.3%; 3d: 38.9%). No effect of resource type is detected on the growth of *G. roeselii* (ANOVA; p=0.705; Mean ± Sd: 0.0125 ± 0.0044 day^{-1}) (data not shown). Three non-exclusive hypotheses can explain the higher mortality of gammarids under aged mask conditions: (1) an impact of microplastics fibres on gammarids as a result of material toxicity (direct effect) and/or obstruction of consumers' digestive tracts (indirect effect), (2) a reduction in the quantity of biofilm present on aged mask discs, leading to mortality due to underfeeding/starvation (quantitative deficiency), (3) a decrease in the food quality of the biofilms developed on the aged substrates (qualitative deficiency).

Analyses of *G. roeselii* gut contents show significant influence of the resource type on gammarid gut filling (ANOVA and post hoc tests; p=0.0155; **Figure 7B**), with a significant 4.7 times-lower filling of *G. roeselii* gut when fed on 3d treated masks (11.4%) compared to those fed on leaf litter (53%). Gut filling of gammarids fed on pristine (35%) and 1d masks (17.8%) is intermediate between that pertaining to organisms fed on leaf litter and 3d masks. Gammarid's gut contents are mainly composed of FPOM and also plastic fibres *albeit* to a much lower proportion (see illustrative pictures in **Figure 7C**). The fractions of microplastic fibres evaluated with respect to the overall gut volume and the effectively occupied gut volume are found *statistically* similar (pristine, 1d & 3d masks; Kruskall-Wallis ANOVA: p>0.05; global mean ± Sd: 1.4±2.6 %; relative mean ± Sd: 7±11.7%). Relative proportion of other items were similar between treatments (Kruskall-Wallis ANOVA: p>0.05).

The above results show that *G. roeselii* feeding on biofilm grown on masks can ingest plastic fibres. As the quantity of plastic fibres ingested by gammarids is similar for the different mask treatments tested, material toxicity (direct toxicity) or gut occlusion (indirect toxicity) by plastic fibre material cannot explain alone the higher mortality of organisms with aged masks (hypothesis (1): toxicity hypothesis rejected). In the current study, aged masks carry biofilms that are less colonized by diatoms and are dominated by bacteria in comparison to pristine masks for which gammarids survival is highest. These results are in agreement with data by Crenier et al. (2017) and Rollin et al. (2018) who reported strong and positive influences of diatoms (a high quality resource) on gammarids survival, growth and reproduction. In their *in situ* study, Labed-Veydert et al. (2022) also confirmed the influence of diatoms-dominated biofilms on survival and growth of macroinvertebrates (including gammarids). Therefore, if the qualitative deficiency hypothesis (hypothesis (3)) seems to be the most relevant one for explaining higher mortality of *G. roeselii* fed with biofilm grown on aged masks, we cannot totally exclude the concomitant influence of quantity deficiency (hypothesis (2)) as gut contents of gammarids are reduced with ageing treatment. This latter point is supported by the fragile nature of the biofilms that may inhibit efficient resource shredding by the gammarids. Finally, concerning the potential role of gammarids as dispersers of plastic fibres, experiments do no evidence significant differences among the various resources considered in terms of number or size of plastic fibre transferred to water (ANOVA: p>0.05; Mean ± Sd: 0.66 ± 0.90 mm): plastic fibre transfer by gammarids in the ecosystem is thus not influenced by mask ageing.

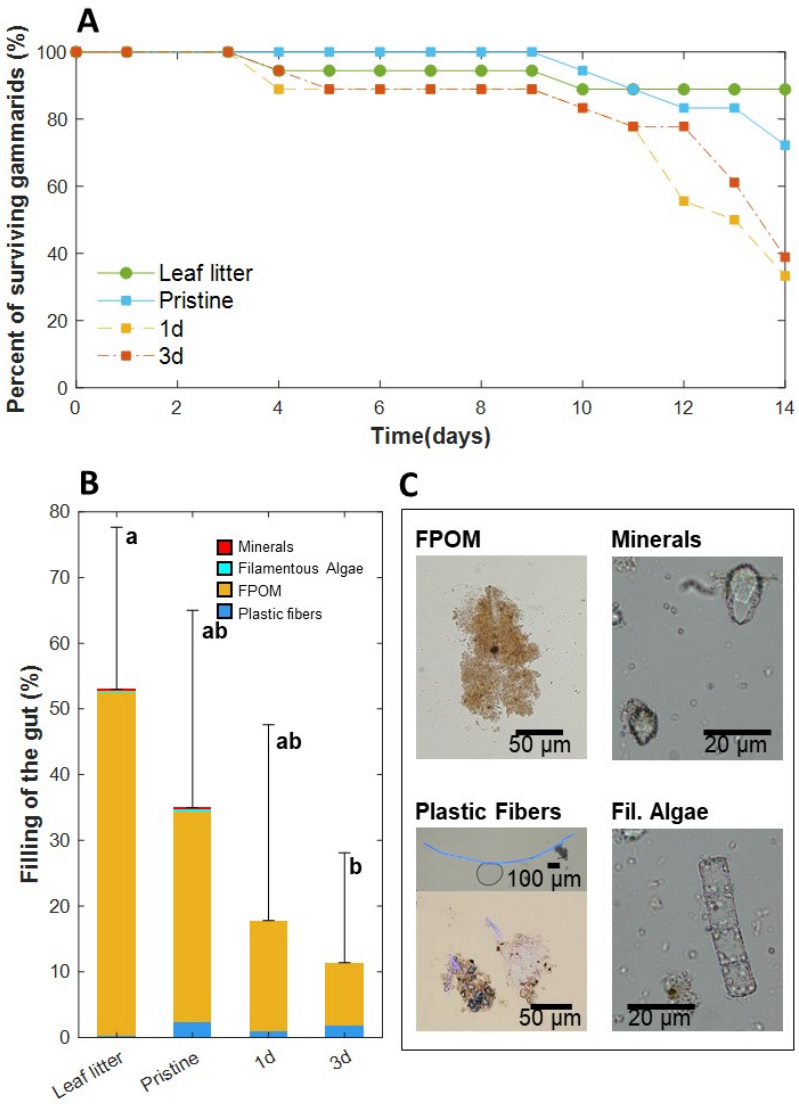

Figure 7. Survival and gut content analysis of *G. roeselii* fed on 4 conditioned resource type: leaf litter (alder), unaged mask (pristine), 1 day (1d) and 3 days (3d) aged mask**. (A)** Kaplan-Meier curves for the time-to-death of organisms fed on the 4 resources type. **(B)** Gut filling and relative proportion of the 4 items found in the gut of gammarids fed on the 4 resources type. Lowercase letters a, ab and b in histograms indicate significant differences ($p<0.05$). **(C)** Example of the items observed in gammarids gut content by optical microscopy. The displayed items correspond to those found at least once in the analysed guts of the gammarids sacrificed at the end of the experiment. Diatoms and CPOM were not found. Size of observed fibres are in agreement with those constituting the 3-layers masks.

4. Conclusions.

Results reported in this work evidence that face masks should be viewed as peculiar plastic waste as they consist of fibres whose surface area well exceeds that of solid plastic objects of equivalent mass. We show that mask photodegradation in its early stage is associated with generation of micron- and nanometre-sized fragments. Surprisingly, the loss of mechanical properties leading to such fragments does not correlate with changes of most of the bulk material properties monitored over time by e.g. X-ray diffraction and infrared spectroscopy. The main changes recorded after UV-exposure involve the production of new chemical groups (carbonyl functions) symptomatic of oxidation process.

For the mask intermediate layer, these newly formed chemical functions are detectable after just a few days of UV-exposure. For all three layers, their quantity is significant at 28 days, as evidenced by the variation in the carbonyl index. Analysis of the colloidal features of released fragments reveals that dispersion of these fragments in 1-250 mM salinity solution is possible even at moderate UV dose (3 days exposure), meaning that mask debris have gained significant polarity. Remarkably, the dependence of electrophoretic mobility of mask debris on salinity features a similar 'banana' shape, regardless of the crystalline form of the polymer and the advancement of the degradation reaction. SEM observations and chemical analysis further reveal the presence of additives in released fibres, especially TiO_2 nanoparticles located both at the surface and in the bulk of the fibres. Fragmentation that follows degradation increases the exposure of these polluting additives towards aquatic biota, a feature that adds to the well-reported issue of fibres ingestion and intestinal damage in living aquatic organisms. This finding is supported by our observation of a change in the distribution of fluorescent entities upon degradation, from homogeneous to heterogeneous in the form of localized blisters at the fibre surface. Reactivity of pristine and photodegraded masks towards aquatic biota is further addressed in terms of organism diversity/abundance in mask-supported biofilms grown in the Moselle River, and survival of gammarids species fed with these biofilms. Overall, mask ageing primarily reduces the abundance of algae (mainly diatoms) and poorly affects both bacteria abundance and microbial community structure. In addition, the mortality of gammarids is found to increase when feeding on biofilms grown on aged masks, mainly because of a deficiency in food resource quality.

Beyond the results briefly summarized above, originality of this work lies in its recourse to a suite of techniques for probing fragments properties versus UV radiation exposure conditions, from the molecular, to colloidal and bulk macroscopic scale. Extensions of this work include additional qualitative and/or quantitative analyses to correlate changes of the different mask properties at short time (i.e. within a few days UV-exposure conditions) with corresponding variations in their colonization by organisms and ecotoxicity effects. Options include the recourse to fluorescence imaging with dedicated molecular probes so as to evaluate hydrophobicity of masks. Establishing firmly specific and mechanistic connections between masks composition/property and effects on biota would further require working with reference samples with simpler chemical composition, like polypropylene particles differing in terms of e.g. organic compounds and inorganic elements.

It is expected that the underlying methodology can be applied to other (potentially) hazardous materials, i.e. all objects made of polypropylene fabrics and found outdoors like big bags employed in the construction sector for waste collection or in the agrifood industry to transport grains, or mulching clothes used in gardens to prevent weed growth.

CRediT authorship contribution statement

I.B.: Conceptualization, Methodology, Validation, Investigation, Writing – original draft, review & editing, Visualization, Supervision, Project administration, Funding acquisition. **R.G.**: Investigation, Supervision. **L.G.**, **A.B.**, **A.R.**, **M.B.**, **D.B.**, **C.B.**, **C.C.**, **P.M.**, **M.Z.**, **F.J.**, **B.G.**, **P.B.**, **C.N.**: Investigation. **M.D.**, **V.F.**: Investigation, Validation, Writing – original draft, Supervision. **C.P.**: Conceptualization, Investigation, Validation, Writing – original draft, Supervision, Funding acquisition. **J.F.L.D.**: Conceptualization, Methodology, Validation, Investigation, Writing – original draft, review & editing, Supervision.

Declaration of Competing Interest

The authors declare that they have no known competing financial interests or personal relationships that could have appeared to influence the work reported in this paper.

Data Availability

Data are available upon requests.

Acknowledgement

This work was financially supported by the Observatoire Terre et Environnement de Lorraine (OTELo) from Nancy, France (Interdisciplinary Project BAlesMAsques). This work was performed with ressources from the Pôle de Compétences en Physico-Chimie de l'Environnement, Pôle de Compétences en Chimie Analytique Environnementale, and Pôle de Compétences en Biologie Environnementale, ANATELo, LIEC laboratory, UMR 7360 CNRS – Université de Lorraine. The LERMAB laboratory (EA 4370-Université de Lorraine) is thanked for providing the accelerated ageing chamber. The scanning electron micrographs were acquired on a microscope of the SCMEM-GEORESSOURCES (UMR 7360 CNRS-Université de Lorraine) with assistance of Andreï Lecomte. Christophe Cloquet from the SARM (CRPG, CNRS-Université de Lorraine) is thanked for his contribution to elemental chemical analysis. WAXS experiments were performed on a diffractometer from the Centre de Compétences X-Gamma (IJL, UMR 7198 CNRS-Université de Lorraine). Maria Cellamare (Phyto-Quality, Paris-France) is thanked for the taxonomic identification of algae in biofilms. Yves Waldvogel (Université de Lorraine, CNRS, LIEC, Nancy-France) is thanked for his contribution to electrokinetic and granulometry experiments.

Appendix A-N. Supporting Information

Supplementary data associated with this article can be found in the online version.

References

Alimi, O.S., Claveau-Mallet, D., Lapointe, M., Biu, T., Liu, L., Hernandez, L.M., Bayen, S., Tufenkji, N., 2023. Effects of weathering on the properties and fate of secondary microplastics from a polystyrene single-use cup. J. Hazard. Mater. 459, 131855.

Al-Malaika, S., Axtell, F., Rothon, R., Gilbert, M., 2017. Chapter 7 - Additives for Plastics. In: Gilbert, M. (Ed.), Brydson's Plastics Materials (Eighth Edition). Butterworth-Heinemann, pp. 127–168.

Almond, J., Sugumaar, P., Wenzel, M.N., Hill, G., Wallis, C., 2020. Determination of the carbonyl index of polyethylene and polypropylene using specified area under band methodology with ATR-FTIR spectroscopy. E-Polym. 20, 369–381.

Ammendolia, J., Saturno, J., Brooks, A.L., Jacobs, S., Jambeck, J.R., 2021. An emerging source of plastic pollution: Environmental presence of plastic personal protective equipment (PPE) debris related to COVID-19 in a metropolitan city. Environ. Pollut. 269, 116160.

Andrady, A.L., 2017. The plastic in microplastics: A review. Mar. Pollut. Bull. 119, 12–22.

Androsch, R., Di Lorenzo, M.L., Schick, C., Wunderlich, B., 2010. Mesophases in polyethylene, polypropylene, and poly(1-butene). Polymer 51, 4639–4662.

Aragaw, T.A., 2020. Surgical face masks as a potential source for microplastic pollution in the COVID-19 scenario. Mar. Pollut. Bull. 159, 111517.

Aranberri-Askargorta, I., Lampke, T., Bismarck, A., 2003. Wetting behavior of flax fibers as reinforcement for polypropylene. J. Colloid Interface Sci. 263, 580–589.

Aslanzadeh, S., Haghighat Kish, M., 2010. Photo-oxidation of polypropylene fibers exposed to short wavelength UV radiations. Fibers Polym. 11, 710–718.

Au, S.Y., Bruce, T.F., Bridges, W.C., Klaine, S.J., 2015. Responses of *Hyalella azteca* to acute and chronic microplastic exposures: Effects of Microplastic Exposure on *Hyalella azteca*. Environ. Toxicol. Chem. 34, 2564–2572.

Benítez, A., Sánchez, J.J., Arnal, M.L., Müller, A.J., Rodríguez, O., Morales, G., 2013. Abiotic degradation of LDPE and LLDPE formulated with a pro-oxidant additive. Polym. Degrad. Stab. 98, 490–501.
Benson, N.U., Bassey, D.E., Palanisami, T., 2021. COVID pollution: impact of COVID-19 pandemic on global plastic waste footprint. Heliyon 7, e06343.
Blais, P., Carlsson, D.J., Wiles, D.M., 1972. Surface changes during polypropylene photo-oxidation: A study by infrared spectroscopy and electron microscopy. J. Polym. Sci. [A1] 10, 1077–1092.
Blarer, P., Burkhardt-Holm, P., 2016. Microplastics affect assimilation efficiency in the freshwater amphipod Gammarus fossarum. Environ. Sci. Pollut. Res. 23, 23522–23532.
Brunauer, S., Emmett, P.H., Teller, E., 1938. Adsorption of Gases in Multimolecular Layers. J. Am. Chem. Soc. 60, 309–319.
Celina, M., George, G.A., Billingham, N.C., 1993. Physical spreading of oxidation in solid polypropylene as studied by chemiluminescence. Polym. Degrad. Stab. 42, 335–344.
Chae, Y., Kim, D., Kim, S.W., An, Y.-J., 2018. Trophic transfer and individual impact of nano-sized polystyrene in a four-species freshwater food chain. Sci. Rep. 8, 284.
Chow, K.Y., Grant, D.J.W., 1988. Surface analysis of griseofulvin powders by krypton adsorption: Evaluation of specific surface area, BET constant C and polanyi adsorption potential. Powder Technol. 56, 209–223.
Chowdhury, H., Chowdhury, T., Sait, S.M., 2021. Estimating marine plastic pollution from COVID-19 face masks in coastal regions. Mar. Pollut. Bull. 168, 112419.
Cooksey, K.E., Wigglesworth-Cooksey, B., 1995. Adhesion of bacteria and diatoms to surfaces in the sea: a review. Aquat. Microb. Ecol.
Crenier, C., Arce-Funck, J., Bec, A., Billoir, E., Perrière, F., Leflaive, J., Guérold, F., Felten, V., Danger, M., 2017. Minor food sources can play a major role in secondary production in detritus-based ecosystems. Freshw. Biol. 62, 1155–1167.
de Sá, L.C., Oliveira, M., Ribeiro, F., Rocha, T.L., Futter, M.N., 2018. Studies of the effects of microplastics on aquatic organisms: What do we know and where should we focus our efforts in the future? Sci. Total Environ. 645, 1029–1039.
Duval, J.F.L., Farinha, J.P.S., Pinheiro, J.P., 2013. Impact of Electrostatics on the Chemodynamics of Highly Charged Metal–Polymer Nanoparticle Complexes. Langmuir 29, 13821–13835.
Duval, J.F.L., Leermakers, F.A.M., van Leeuwen, H.P., 2004. Electrostatic Interactions between Double Layers: Influence of Surface Roughness, Regulation, and Chemical Heterogeneities. Langmuir 20, 5052–5065.
Duval, J.F.L., Ohshima, H., 2006. Electrophoresis of Diffuse Soft Particles. Langmuir 22, 3533–3546.
Felske, A., Akkermans, A.D.L., De Vos, W.M., 1998. Quantification of 16S rRNAs in Complex Bacterial Communities by Multiple Competitive Reverse Transcription-PCR in Temperature Gradient Gel Electrophoresis Fingerprints. Appl. Environ. Microbiol. 64, 4581–4587.
Felten, V., Tixier, G., Gué Rold, F., De Crespin De Billy, V., Dangles, O., 2008. Quantification of diet variability in a stream amphipod: implications for ecosystem functioning. Fundam. Appl. Limnol. 170, 303–313.
Felten, V., Toumi, H., Masfaraud, J.-F., Billoir, E., Camara, B.I., Férard, J.-F., 2020. Microplastics enhance Daphnia magna sensitivity to the pyrethroid insecticide deltamethrin: Effects on life history traits. Sci. Total Environ. 714, 136567.
Ferreira, I., Venâncio, C., Lopes, I., Oliveira, M., 2019. Nanoplastics and marine organisms: What has been studied? Environ. Toxicol. Pharmacol. 67, 1–7.
Fries, E., Dekiff, J.H., Willmeyer, J., Nuelle, M.-T., Ebert, M., Remy, D., 2013. Identification of polymer types and additives in marine microplastic particles using pyrolysis-GC/MS and scanning electron microscopy. Environ. Sci. Process. Impacts 15, 1949.
Gigault, J., Halle, A. ter, Baudrimont, M., Pascal, P.-Y., Gauffre, F., Phi, T.-L., El Hadri, H., Grassl, B., Reynaud, S., 2018. Current opinion: What is a nanoplastic? Environ. Pollut. 235, 1030–1034.
Goikhman, A.S., Kirichenko, V.I., Budnitskii, G.A., 1984. X-Ray diffraction measurements of the crystallinity of polypropylene fibres. Polym. Sci. USSR 26, 974–981.

Gooch, J.W., 2002. Analysis and Deformulation of Polymeric Materials, Topics in Applied Chemistry. Kluwer Academic Publishers, Boston.
Gopmandal, P.P., Duval, J.F.L., 2022. Electrostatics and electrophoresis of engineered nanoparticles and particulate environmental contaminants: Beyond zeta potential-based formulation. Curr. Opin. Colloid Interface Sci. 60, 101605.
Guo, Y., Liu, Y., Xiang, T., Li, J., Lv, M., Yan, Y., Zhao, J., Sun, J., Yang, X., Liao, C., Fu, J., Shi, J., Qu, G., Jiang, G., 2023. Disposable Polypropylene Face Masks: A Potential Source of Micro/Nanoparticles and Organic Contaminates in Humans. Environ. Sci. Technol. 57, 5739–5750.
Hu, T., Shen, M., Tang, W., 2022. Wet wipes and disposable surgical masks are becoming new sources of fiber microplastic pollution during global COVID-19. Environ. Sci. Pollut. Res. 29, 284–292.
Hughes, R.H., 1969. The determination of the isotacticity of polypropylene in the 90–100% range by infrared spectroscopy. J. Appl. Polym. Sci. 13, 417–425.
Isasi, J.R., Mandelkern, L., Galante, M.J., Alamo, R.G., 1999. The degree of crystallinity of monoclinic isotactic poly(propylene). J. Polym. Sci. Part B Polym. Phys. 37, 323–334.
Ismail, M.F., Islam, M.A., Khorshidi, B., Sadrzadeh, M., 2021. Prediction of surface charge properties on the basis of contact angle titration models. Mater. Chem. Phys. 258, 123933.
Jacobasch, H.-J., 1984. Characterization of the adhesion properties of polymers by electrokinetic measurements. Angew. Makromol. Chem. 128, 47–69.
Klindworth, A., Pruesse, E., Schweer, T., Peplies, J., Quast, C., Horn, M., Glöckner, F.O., 2013. Evaluation of general 16S ribosomal RNA gene PCR primers for classical and next-generation sequencing-based diversity studies. Nucleic Acids Res. 41, e1.
Košíková, B., Revajová, A., Demianová, V., 1995. The effect of adding lignin on modification of surface properties of polypropylene. Eur. Polym. J. 31, 953–956.
Kotek, J., Kelnar, I., Baldrian, J., Raab, M., 2004. Structural transformations of isotactic polypropylene induced by heating and UV light. Eur. Polym. J. 40, 2731–2738.
Labed-Veydert, T., Danger, M., Felten, V., Bec, A., Laviale, M., Cellamare, M., Desvilettes, C., 2022. Microalgal food sources greatly improve macroinvertebrate growth in detritus-based headwater streams: Evidence from an instream experiment. Freshw. Biol. 67, 1380–1394.
Lacoste, J., Vaillant, D., Carlsson, D.J., 1993. Gamma-, photo-, and thermally-initiated oxidation of isotactic polypropylene. J. Polym. Sci. Part Polym. Chem. 31, 715–722.
Lambert, S., Scherer, C., Wagner, M., 2017. Ecotoxicity testing of microplastics: Considering the heterogeneity of physicochemical properties: Ecotoxicity Testing of Microplastics. Integr. Environ. Assess. Manag. 13, 470–475.
Lambert, S., Wagner, M., 2016. Formation of microscopic particles during the degradation of different polymers. Chemosphere 161, 510–517.
Lee, Q.Y., Li, H., 2021. Photocatalytic Degradation of Plastic Waste: A Mini Review. Micromachines 12, 907.
Lima, M.F.S., Vasconcellos, M.A.Z., Samios, D., 2002. Crystallinity changes in plastically deformed isotactic polypropylene evaluated by x-ray diffraction and differential scanning calorimetry methods. J. Polym. Sci. Part B Polym. Phys. 40, 896–903.
Liu, X., Cao, W., Xie, L., Sun, C., Jiang, F., 2022. Photoaging Characteristics of Disposable Masks under UV Irradiation. J. Mar. Sci. Eng. 10, 170.
Lund, J.W.G., Kipling, C., Le Cren, E.D., 1958. The inverted microscope method of estimating algal numbers and the statistical basis of estimations by counting. Hydrobiologia 11, 143–170.
Luongo, J.P., 1960. Infrared study of polypropylene. J. Appl. Polym. Sci. 3, 302–309.
Ma, J., Chen, F., Xu, H., Jiang, H., Liu, J., Li, P., Chen, C.C., Pan, K., 2021. Face masks as a source of nanoplastics and microplastics in the environment: Quantification, characterization, and potential for bioaccumulation. Environ. Pollut. 288, 117748.
Ma, J., Chen, F., Xu, H., Liu, J., Chen, C.C., Zhang, Z., Jiang, H., Li, Y., Pan, K., 2022. Fate of face masks after being discarded into seawater: Aging and microbial colonization. J. Hazard. Mater. 436, 129084.

Machado, G., Denardin, E.L.G., Kinast, E.J., Gonçalves, M.C., de Luca, M.A., Teixeira, S.R., Samios, D., 2005. Crystalline properties and morphological changes in plastically deformed isotatic polypropylene evaluated by X-ray diffraction and transmission electron microscopy. Eur. Polym. J. 41, 129–138.

Mateos-Cárdenas, A., O'Halloran, J., van Pelt, F.N.A.M., Jansen, M.A.K., 2020. Rapid fragmentation of microplastics by the freshwater amphipod Gammarus duebeni (Lillj.). Sci. Rep. 10, 12799.

Men, C., Liu, R., Xu, F., Wang, Q., Guo, L., Shen, Z., 2018. Pollution characteristics, risk assessment, and source apportionment of heavy metals in road dust in Beijing, China. Sci. Total Environ. 612, 138–147.

Morgana, S., Casentini, B., Amalfitano, S., 2021. Uncovering the release of micro/nanoplastics from disposable face masks at times of COVID-19. J. Hazard. Mater. 419, 126507.

Muller, E.I., Souza, J.P., Muller, C.C., Muller, A.L.H., Mello, P.A., Bizzi, C.A., 2016. Microwave-assisted wet digestion with H2O2 at high temperature and pressure using single reaction chamber for elemental determination in milk powder by ICP-OES and ICP-MS. Talanta 156–157, 232–238.

Natta, G., Corradini, P., 1960. Structure and Properties of Isotactic Polyprolylene. Nuovo Cimento Suppl 40–51.

Nishida, K., Okada, K., Asakawa, H., Matsuba, G., Ito, K., Kanaya, T., Kaji, K., 2012. In situ observations of the mesophase formation of isotactic polypropylene—A fast time-resolved X-ray diffraction study. Polym. J. 44, 95–101.

Oehlmann, J., Schulte-Oehlmann, U., Kloas, W., Jagnytsch, O., Lutz, I., Kusk, K.O., Wollenberger, L., Santos, E.M., Paull, G.C., Van Look, K.J.W., Tyler, C.R., 2009. A critical analysis of the biological impacts of plasticizers on wildlife. Philos. Trans. R. Soc. B Biol. Sci. 364, 2047–2062.

Ogonowski, M., Schür, C., Jarsén, Å., Gorokhova, E., 2016. The Effects of Natural and Anthropogenic Microparticles on Individual Fitness in Daphnia magna. PLOS ONE 11, e0155063.

Ohtani, B., Adzuma, S., Miyadzu, H., Nishimoto, S., Kagiya, T., 1989. Photocatalytic degradation of polypropylene film by dispersed titanium dioxide particles. Polym. Degrad. Stab. 23, 271–278.

Parashar, N., Hait, S., 2021. Plastics in the time of COVID-19 pandemic: Protector or polluter? Sci. Total Environ. 759, 144274.

Patrício Silva, A.L., Prata, J.C., Walker, T.R., Campos, D., Duarte, A.C., Soares, A.M.V.M., Barcelò, D., Rocha-Santos, T., 2020. Rethinking and optimising plastic waste management under COVID-19 pandemic: Policy solutions based on redesign and reduction of single-use plastics and personal protective equipment. Sci. Total Environ. 742, 140565.

Pereira, L.S.F., Pedrotti, M.F., Miceli, T.M., Pereira, J.S.F., Flores, E.M.M., 2016. Determination of elemental impurities in poly(vinyl chloride) by inductively coupled plasma optical emission spectrometry. Talanta 152, 371–377.

Philippart, J.-L., Sinturel, C., Arnaud, R., Gardette, J.-L., 1999. Influence of the exposure parameters on the mechanism of photooxidation of polypropylene. Polym. Degrad. Stab. 13.

Philippart, J.-L., Sinturel, C., Gardette, J.-L., 1997. Influence of light intensity on the photooxidation of polypropylene. Polym. Degrad. Stab. 58, 261–268.

Prata, J.C., Silva, A.L.P., Walker, T.R., Duarte, A.C., Rocha-Santos, T., 2020. COVID-19 Pandemic Repercussions on the Use and Management of Plastics. Environ. Sci. Technol. 54, 7760–7765.

Qiao, R., Deng, Y., Zhang, S., Wolosker, M.B., Zhu, Q., Ren, H., Zhang, Y., 2019. Accumulation of different shapes of microplastics initiates intestinal injury and gut microbiota dysbiosis in the gut of zebrafish. Chemosphere 236, 124334.

R Core Team, 2019. A Language and Environment for Statistical Computing. R Foundation for Statistical Computing, https://www.R-project.org/.

Rao, T.S., Rani, P.G., Venugopalan, V.P., Nair, K.V.K., 1997. Biofilm formation in a freshwater environment under photic and aphotic conditions. Biofouling 11, 265.

Rathinamoorthy, R., Balasaraswathi, S.R., 2022. Disposable tri-layer masks and microfiber pollution – An experimental analysis on dry and wet state emission. Sci. Total Environ. 816, 151562.

Ren, Z., Shanks, R.A., Rook, T.J., 2002. Processing and Properties of Polypropylene Composites with High Filler Content. Polym. Compos. 10, 10.

Rochman, C.M., Hoh, E., Hentschel, B.T., Kaye, S., 2013. Long-Term Field Measurement of Sorption of Organic Contaminants to Five Types of Plastic Pellets: Implications for Plastic Marine Debris. Environ. Sci. Technol. 47, 1646–1654.

Rollin, M., Coulaud, R., Danger, M., Sohm, B., Flayac, J., Bec, A., Chaumot, A., Geffard, O., Felten, V., 2018. Additive effect of calcium depletion and low resource quality on Gammarus fossarum (Crustacea, Amphipoda) life history traits. Environ. Sci. Pollut. Res. Int. 25, 11264–11280.

Rouillon, C., Bussiere, P.-O., Desnoux, E., Collin, S., Vial, C., Therias, S., Gardette, J.-L., 2016. Is carbonyl index a quantitative probe to monitor polypropylene photodegradation? Polym. Degrad. Stab. 128, 200–208.

Saliu, F., Veronelli, M., Raguso, C., Barana, D., Galli, P., Lasagni, M., 2021. The release process of microfibers: from surgical face masks into the marine environment. Environ. Adv. 4, 100042.

Severini, F., Gallo, R., Ipsale, S., 1988. Environmental degradation of polypropylene. Polym. Degrad. Stab. 22, 185–194.

Shrivastava, A., 2018. 4 - Additives for Plastics. In: Shrivastava, A. (Ed.), Introduction to Plastics Engineering, Plastics Design Library. William Andrew Publishing, pp. 111–141.

Škvarla, J., 2007. Hard versus Soft Particle Electrokinetics of Silica Colloids. Langmuir 23, 5305–5314.

Slepička, P., Vasina, A., Kolská, Z., Luxbacher, T., Malinský, P., Macková, A., Švorčík, V., 2010. Argon plasma irradiation of polypropylene. Nucl. Instrum. Methods Phys. Res. Sect. B Beam Interact. Mater. At., 19th International Conference on Ion Beam Analysis 268, 2111–2114.

Song, J., Duval, J.F.L., Cohen Stuart, M.A., Hillborg, H., Gunst, U., Arlinghaus, H.F., Vancso, G.J., 2007. Surface Ionization State and Nanoscale Chemical Composition of UV-Irradiated Poly(dimethylsiloxane) Probed by Chemical Force Microscopy, Force Titration, and Electrokinetic Measurements. Langmuir 23, 5430–5438.

STATISTA, 2022. Face Masks - Worldwide | Statista Market Forecast [WWW Document]. URL https://www.statista.com/outlook/cmo/tissue-hygiene-paper/face-masks/worldwide (accessed 12.13.22).

Wang, Z., An, C., Chen, X., Lee, K., Zhang, B., Feng, Q., 2021. Disposable masks release microplastics to the aqueous environment with exacerbation by natural weathering. J. Hazard. Mater. 417, 126036.

WHO, 2021. When and how to use masks [WWW Document]. URL https://www.who.int/emergencies/diseases/novel-coronavirus-2019/advice-for-public/when-and-how-to-use-masks (accessed 1.6.23).

Wright, R.J., Erni-Cassola, G., Zadjelovic, V., Latva, M., Christie-Oleza, J.A., 2020. Marine Plastic Debris: A New Surface for Microbial Colonization. Environ. Sci. Technol. 54, 11657–11672.

Wright, S.L., Thompson, R.C., Galloway, T.S., 2013. The physical impacts of microplastics on marine organisms: A review. Environ. Pollut. 178, 483–492.

Wu, P., Li, J., Lu, X., Tang, Y., Cai, Z., 2022. Release of tens of thousands of microfibers from discarded face masks under simulated environmental conditions. Sci. Total Environ. 806, 150458.

Zimmermann, R., Dukhin, S., Werner, C., 2001. Electrokinetic Measurements Reveal Interfacial Charge at Polymer Films Caused by Simple Electrolyte Ions. J. Phys. Chem. B 105, 8544–8549.

APPENDIX - Supporting Information

Photodegradation of disposable polypropylene face masks: physicochemical properties of debris and implications for the toxicity of mask-carried river biofilms.

Isabelle Bihannic,[a,*] Renaud Gley,[a] Lucas Gallo,[a] Apolline Badura,[a] Angelina Razafitianamaharavo,[a] Maximilien Beuret,[b] David Billet,[a] Clément Bojic,[b] Céline Caillet,[a] Philippine Morlot,[b] Marie Zaffino,[b] Fatina Jouni,[b] Béatrice George,[c] Pascal Boulet,[d] Camille Noûs,[e] Michael Danger,[b] Vincent Felten,[b] Christophe Pagnout,[b] Jérôme F.L. Duval[a,*]

a. Université de Lorraine, CNRS, LIEC, F-54000 Nancy, France.
b. Université de Lorraine, CNRS, LIEC, F-57000 Metz, France.
c. Université de Lorraine, INRAE, LERMAB, F-54000 Nancy, France.
d. Université de Lorraine, CNRS, IJL, F-54000 Nancy, France.
e. Cogitamus Laboratory, Paris, France.

* Corresponding authors. Email: isabelle.bihannic@univ-lorraine.fr, jerome.duval@univ-lorraine.fr

This document contains 23 pages and 17 supplementary figures and 1 supplementary table.

OUTLINE.

A. Materials and Methods

Preamble. The question of the very significance of reporting standard deviations for the different indexes (CI_X, HC_{IR} and CaI_{IR}) provided in **Table 1** (in main text) for the bulk properties of polypropylene masks is debatable, as judged by previous studies/comments published in journals focusing on polymer chemistry and degradation. In particular, concerning carbonyl index, Celina et al. (2021) extensively details the ''significant error margins in carbonyl quantification, with exact carbonyl species and extinction coefficients already being major contributors on their own''. The authors further argue that ''experimental variances depend on the combination of uncertainty in exact carbonyl species, extinction coefficient, contributions from neighboring convoluting peaks, matrix interaction phenomena and instrumental variations in primary IR spectral acquisition (refractive index and penetration depth for ATR measurements)''. Given the inherent heterogeneity of composition of pristine masks from one sample to another, and the obvious heterogeneity of masks composition/structure brought by photodegradation process from molecular to macroscopic scale (cf. e.g. **Figures 2,** and **Figures C.1(b) and E.3** in this **Supporting Information**), a question to be asked is how many mask samples must be tested to provide statistically meaningful standard deviation information. That question has no obvious answer. Probably the amount of required pristine masks (subsequently subjected to UV treatment) to be tested should be sufficiently large so as to cover the entire spectrum of heterogeneities of their physicochemical and elemental composition properties, i.e. surely more than N=3 or 4, and most probably a few hundreds or more, that is the amount typically considered to check reproducibility of large-scale mask production. Accordingly, and given the costs of the multi-technique measurements we provide, it is not practically feasible and scientifically meaningful to provide statistically relevant standard deviations for the indexes pertaining to bulk mask properties (CI_X, HC_{IR} and CaI_{IR}).

Wide Angle X-ray scattering (WAXS).

Wide angle X-ray scattering pattern were recorded with a 2D BRUKER APEX II detector. Obtained images of dimension 512×512 pixels (pixel size of 75×75 µm², binning of 8) were collected with a 60 s acquisition time. Samples were positioned at the centre of the goniometer with help of a goniometer head. The mechanical strength of most of the photodegraded materials made it possible to stack 4 layers at the centre of the sample-holder. For the most degraded samples (i.e. after 28 days of UV treatment), two Kapton windows were required to close the sample holder. Scattering from the background (air and/or Kapton windows) was recorded and removed after transmission correction. One-dimensional diffraction curves were calculated from the two-dimensional WAXS patterns according to an angular averaging procedure.

Data processing consisted in decomposing the whole WAXS diagram on the angular domain covering the 11 to 24-2θ degrees range. The experimental curves were decomposed into the sum of peaks associated with crystallized phases, plus an additional contribution corresponding to the amorphous halo. Each peak marking the presence of a crystallized phase was fitted to a pseudo-Voigt function, and the amorphous halo was adjusted to a split Gaussian component. Data were analysed using the open-source fitting software Fityk (Wojdyr, 2010).

Fourier Transform Infrared spectroscopy (FTIR).

For pristine mask specimens (unexposed to UV) and short time UV-treated specimens (1, 2 or 3 days), fibers were pulled out from layers with tweezers. Approximately 1 mg of the fibre samples was sandwiched homogeneously between two layers of ground KBr powder of 100 mg each (Reference

221864-25G FT-IR, grade ≥ 99% trace metals basis, SIGMA-MERCK) and compressed to form 13 mm diameter pellets. For mask layers highly degraded by UV exposition (e.g. after 28 days in the QUV tester), around 1 mg of powdery samples was mixed with KBr powder and ground in an agate mortar before compression in 13 mm pellets.

Gas adsorption.

Gas adsorption experiments were conducted using krypton. The choice of this gas probe as adsorbate is motivated by the expected small SSA of the materials of interest in this work. Prior to adsorption measurement, about 250 mg of samples was outgassed overnight at 60°C under turbo pump vacuum, until a vacuum of 10^{-5} Pa was achieved. High Purity Krypton (Kr N48, purity > 99.995%) used for the experiments was provided by Alphagaz (France). Specific surface areas were estimated on the basis of the Brunauer-Emmet-Teller (BET) equation (Brunauer et al., 1938) adopting 21 $Å^2$ for the effective cross-sectional area occupied by an adsorbed krypton atom (Sing, 1985). The relative pressure window used for the calculation ranges from 0.05 to 0.3. Regular analyses performed on a certified reference material (SiO_2 BAM-PM-101 purchased from the Federal Institute for Materials Research and Testing, Germany) with a SSA of 0.177 ± 0.004 m^2g^{-1} led to a 0.02 m^2g^{-1} precision on that sample.

Atomic Force Microscopy (AFM).

A few drops of ethanol suspension containing mask fragments were deposited onto a cleaned borosilicate glass slide and immediately dried at ambient temperature. AFM probes used for measurements were NPG Silicon Nitride tips (30 nm apex curvature radius) with nominal spring constant value 0.32 ± 0.2 N/m.

Electrokinetics.

Suspensions were prepared for electrokinetic measurements by collecting 18 mg of photodegraded mask debris and dispersing them into 80 mL of a so-called 'very soft' water. The very soft water was prepared by adding 24 mg of $NaHCO_3$, 15 mg of $CaSO_4$ and $MgSO_4$, and 1 mg of KCl to 2 L of ultra-pure water. Prior to electrophoretic mobility measurements, the debris suspension (pH 7.35) was agitated for 1 hour on a rocking table. The first point of the mobility versus [KNO_3] curve was recorded on this suspension. Then, KNO_3 salt concentration in the debris suspension was varied upon proper addition of 2 M KNO_3 aliquots so as to reach a solution ionic strength we varied in the range 0.57 mM (ionic strength of very soft water) to 250 mM. In a last series of experiments, we measured the dependence of the electrophoretic mobility of plastic debris on solution pH (3 to 10) adjusted with proper addition of 1 M HNO_3 solution (one batch, pH 7 to 3) or 1 M NaOH solution (second batch, pH 7 to 10) in 12 mM KNO_3 solution.

***16S rRNA gene quantification*.**

The qPCR reactions were performed in 20 µL with 400 nM reverse and forward primers, 0.6 µg/µL BSA, 1% dimethylsulfoxide, 10 µL Fast SYBR Green master mix (Invitrogen) and 2 µL of extracted DNA at 2.5 ng/µl, or 1 µL of linear plasmid used as standard or milliQ water for negative control. Amplification conditions were 30 s at 95°C and 40 cycles of 95°C for 30 s, 30 s at 60°C, and 72°C for 30 s, followed by a final extension of 7 min at 72°C. Melting curves were generated from 52°C to 95°C with an increase of 0.5°C every 5 s. For each sample, melting curves were manually checked to verify amplification specificity. A standard curve was constructed from a 10-fold serial dilution (10^9 to 10^1 gene copies per µL) of PstI linearized pJET1.2 plasmids containing the 16S rRNA gene of *E. coli* JM109.

Toxicity assay.

All food resource discs were freeze-dried and weighed to the nearest 0.01 mg (with a Perkin Elmer AD6 Autobalance) before and after being offered to gammarids. A set of 72 juvenile *G. roeseli* was sorted according to their body length and was photographed under a stereomicroscope (×6 to ×40 magnification) in their curved state. Length was recorded from the base of the first antenna to the base of the telson (carried by the third uromere) by following the upper part of the pereiomere using SigmaScan Image Analysis Version 5.000 (SPSS Inc, Chicago, IL, USA; linear state = 0.88 × curved state [mm]; $R^2 = 0.98$). Initial total body length of gammarids did not differ between the 4 tested conditions (mean size ± SD: 5.07 ± 0.66 mm; $F_{3,68} = 0.45$; $p > 0.05$; one-way ANOVA). Juvenile gammarids were randomly transferred in replicates to initiate the experiment.

B. Experimental set-up for mask exposure in the Moselle River.

Figure B.1. Masks were sandwiched between two transparent polymethyl methacrylate sheets. The upper sheet was openwork to allow mask colonization by microorganisms during exposure in the river. This experimental device was weighted and horizontally immersed in the Moselle River for 4 weeks.

C. Aspect of masks after photodegradation.

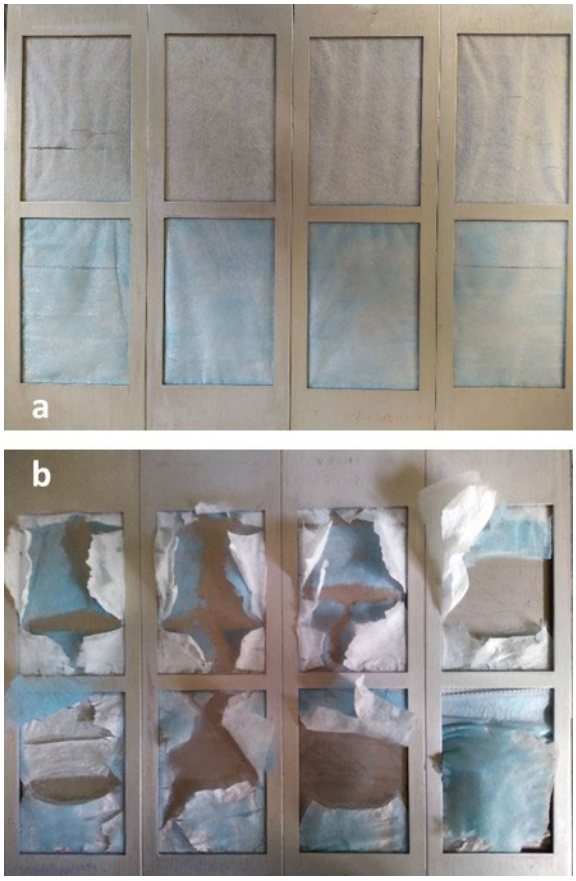

Figure C.1 Aspects of masks on sample holders immediately after their removal from the UV-ageing chamber. The size of the opening in the sample holder is 6 cm×9 cm. **(a)**: masks after 3 days UV-exposure. **(b)**: masks after 28 days UV-exposure.

D. Complementary Wide Angle X-ray Scattering (WAXS) results.

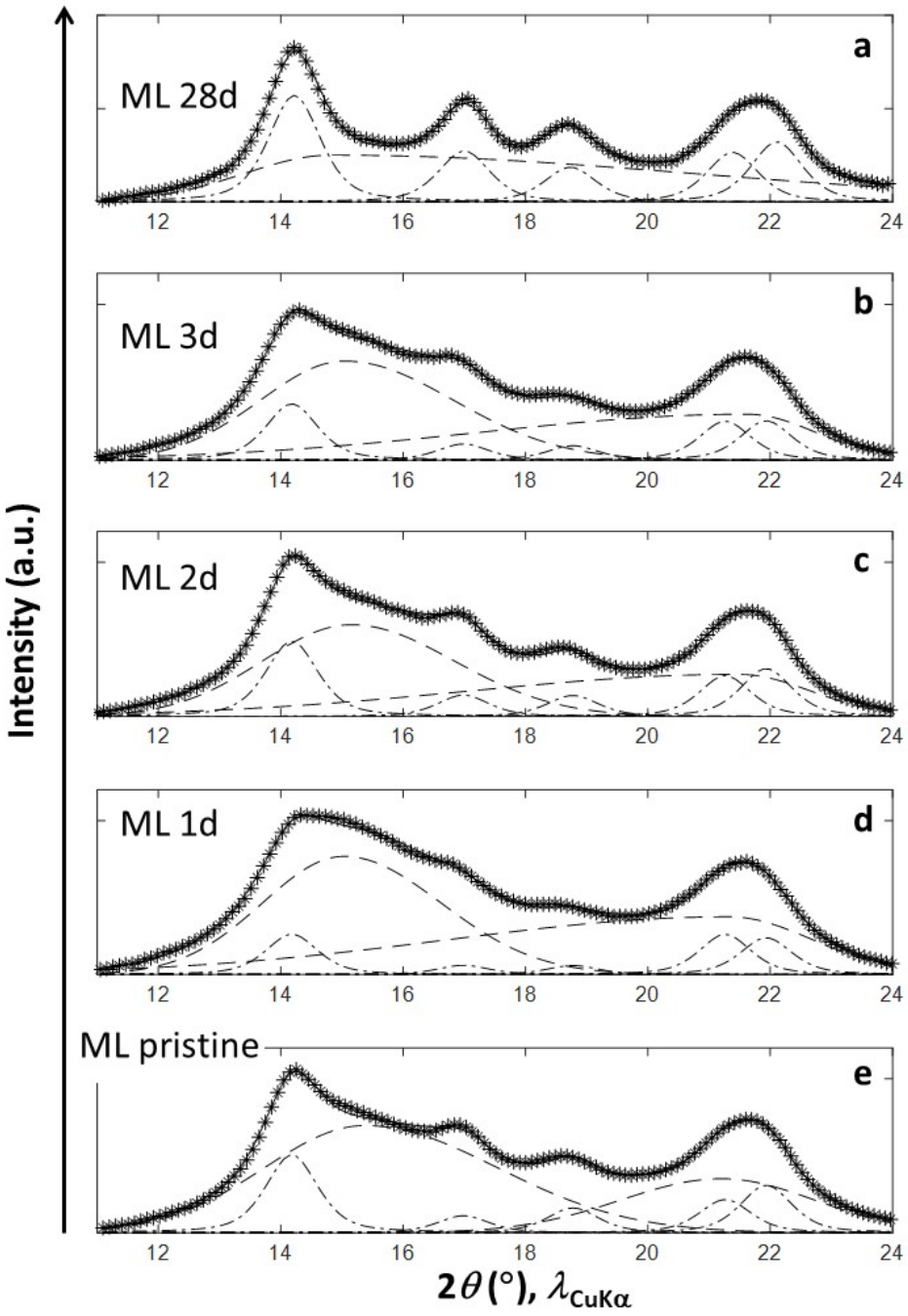

Figure D.1. Decomposition of the Wide-Angle X-rays Scattering (WAXS) curves recorded for the middle layer (ML) in pristine state or after ageing (indicated). For UV exposure duration shorter or equal to 3 days ((**b)** to **(e**)), each experimental curve (-*-) is decomposed using 5 contributing peaks at fixed angular positions (indicated) corresponding to the α-monoclinic phase, plus two additional broad contributions (indicated) corresponding to the amorphous phase.

E. Complementary Scanning Electron Microscopy (SEM) results.

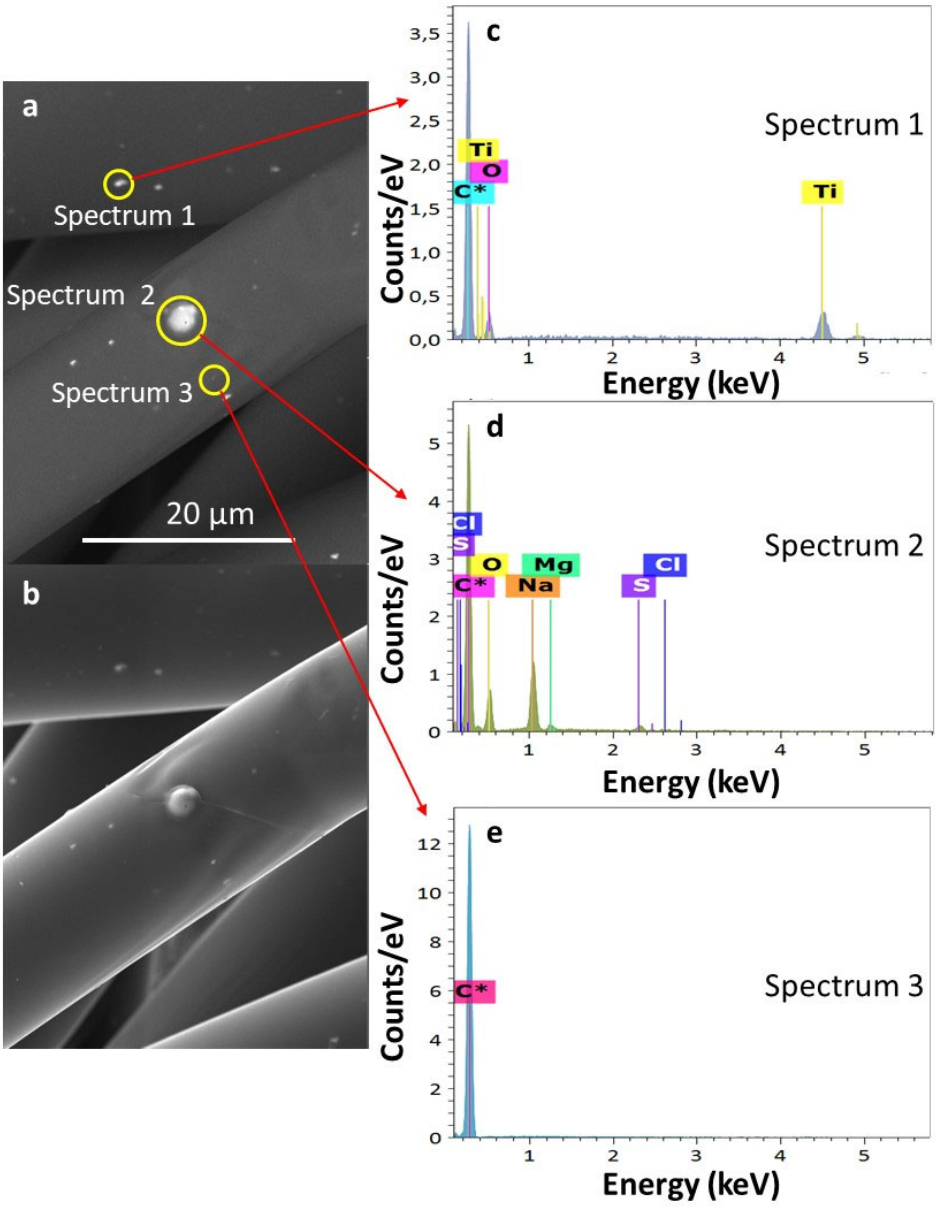

Figure E.1. (a) Illustrative Scanning electron micrographs (SEM) of pristine inner layer (IL). **(b)** Detection of backscattered electrons (BSE) corresponding to **(a)**. **(c)-(e)** Detection of secondary electrons (SE) (corresponding analysed areas are identified in **(a)**) and elemental analysis by energy dispersive X-ray spectroscopy (EDS). Ca element was also detected in some of the spectra corresponding to the condition in panel (d).

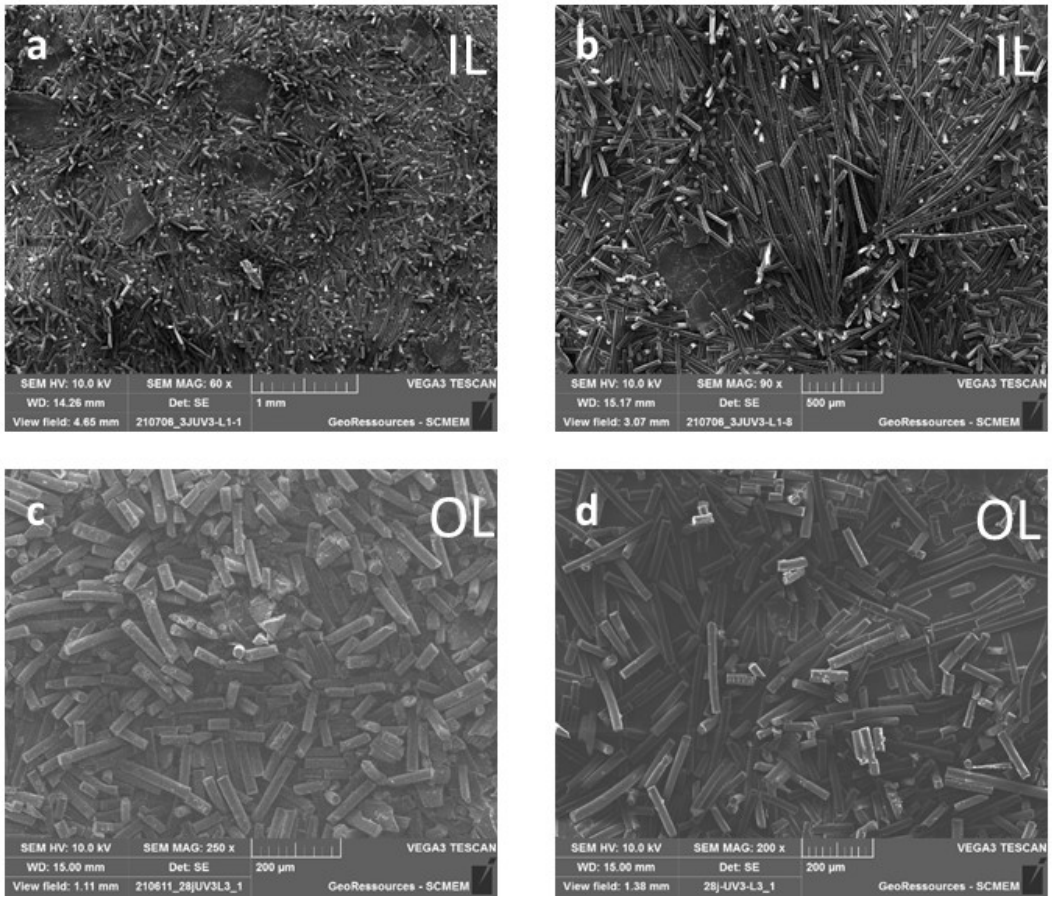

Figure E.2. Scanning electron micrographs of 3 days UV-exposed inner layer (**(a)-(b)**) and outer layer (**(c)-(d**)). Micrographs correspond to secondary electrons (SE) detection mode.

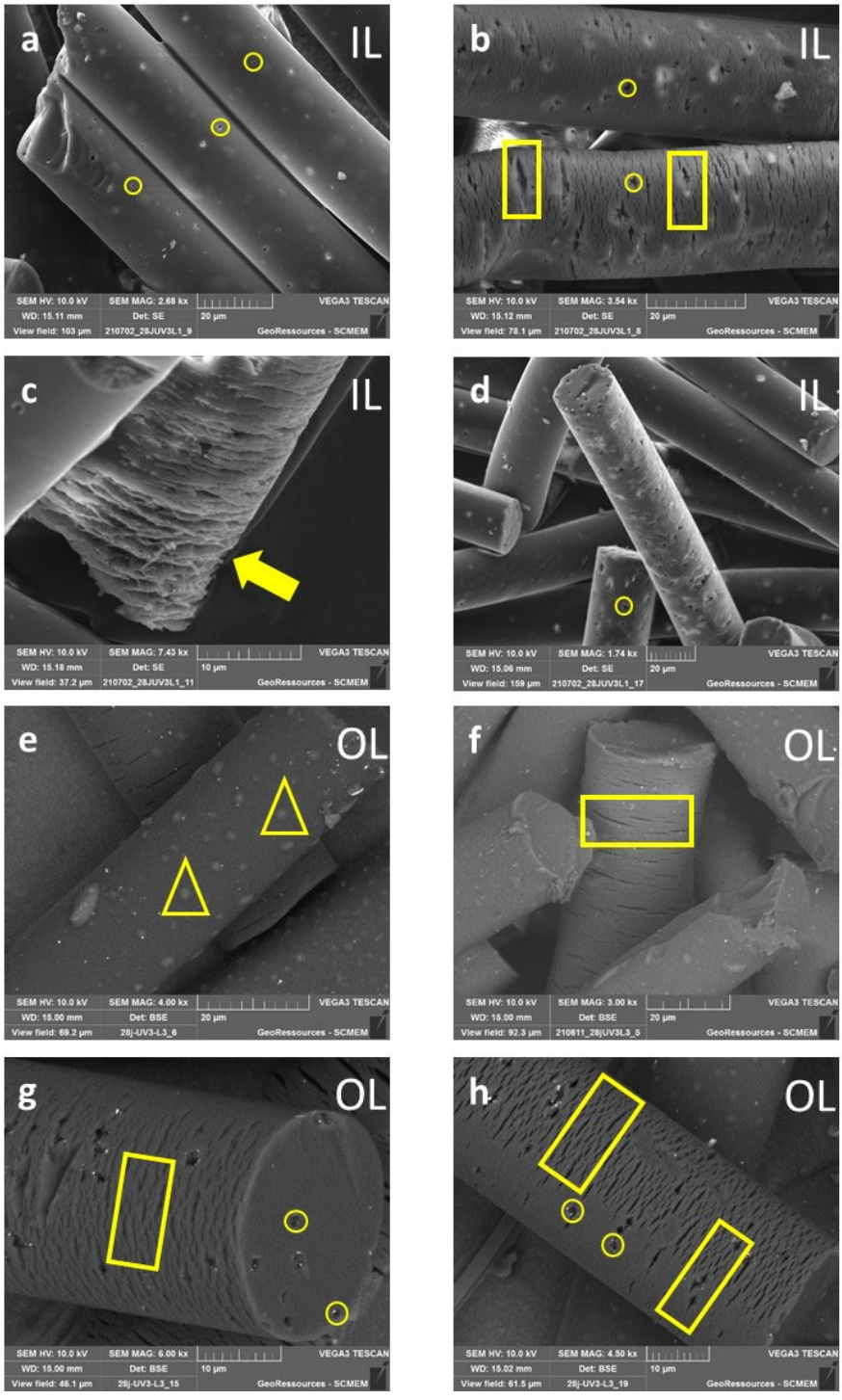

Figure E.3. Scanning electron micrographs of 28 days UV-exposed inner and outer layers (IL and OL, indicated). Illustration for the presence of cavities (circles), cracks (rectangles), blisters (diamonds) and laminated texture (arrows). For the sake of clarity, only some of the most characteristic defaults are highlighted here. BSE: backscattered electrons – SE: secondary electrons. See main text for details.

F. Complementary Atomic Force Microscopy (AFM) results.

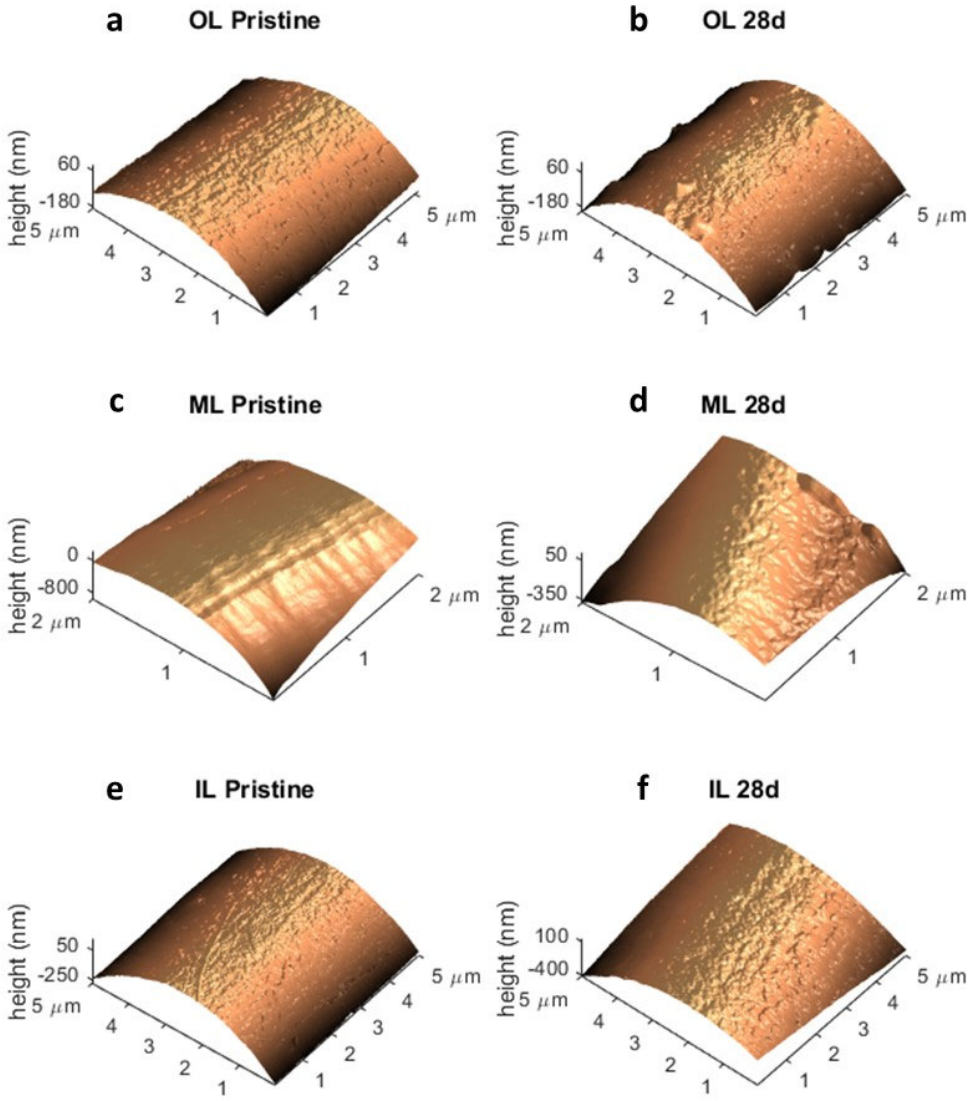

Figure F.1. Representative AFM height sensor images for the outer layer (OL, **(a)-(b)**), middle layer (ML, **(c)-(d)**) and inner layer (IL, **(e)-(f)**), in pristine state (no UV exposure) or after 28 days UV exposure (28d) (indicated). The size of the images is scaled according to the fibre diameters, i.e. images of 5x5 µm for the inner and outer layers, and 2x2 µm for the middle layer. AFM images shown here are those where roughness evaluation was performed (cf. Table 1 in the main text).

G. Complementary gas adsorption results.

In order to address the possible impact of generated cracks on BET results, we computed theoretical SSA for materials consisting of an ensemble of cylinders defined by different lengths and diameters **(Figure G.1)**. Considering a density (*d*) of 0.9 g cm^{-3}, the obtained specific surface area of 50 µm-long cylinder was ca. 0.6, 0.32 and 0.27 m^2 g^{-1} for a radius of 4, 8 and 10 µm, respectively, in agreement with results derived from BET measurements. For a cylinder length above a threshold value of a few hundreds of microns, the calculated SSA reached asymptotically a plateau whose value corresponded to the contribution of the lateral surface to the whole SSA (situation of an infinite cylinder). Indeed, for cylinders of radius *R* and length *L*, SSA has 2 components, one associated with the 2 basal surfaces and the other with the cylinder lateral surface. These components contribute to the total SSA according to 2/(*dL*) and 2/(*dR*), respectively. This demonstrates that for debris with sufficiently large aspect ratio, the contribution of lateral surfaces in the overall SSA overwhelms that from basal surfaces. In turn, cracks do not contribute much to the overall SSA.

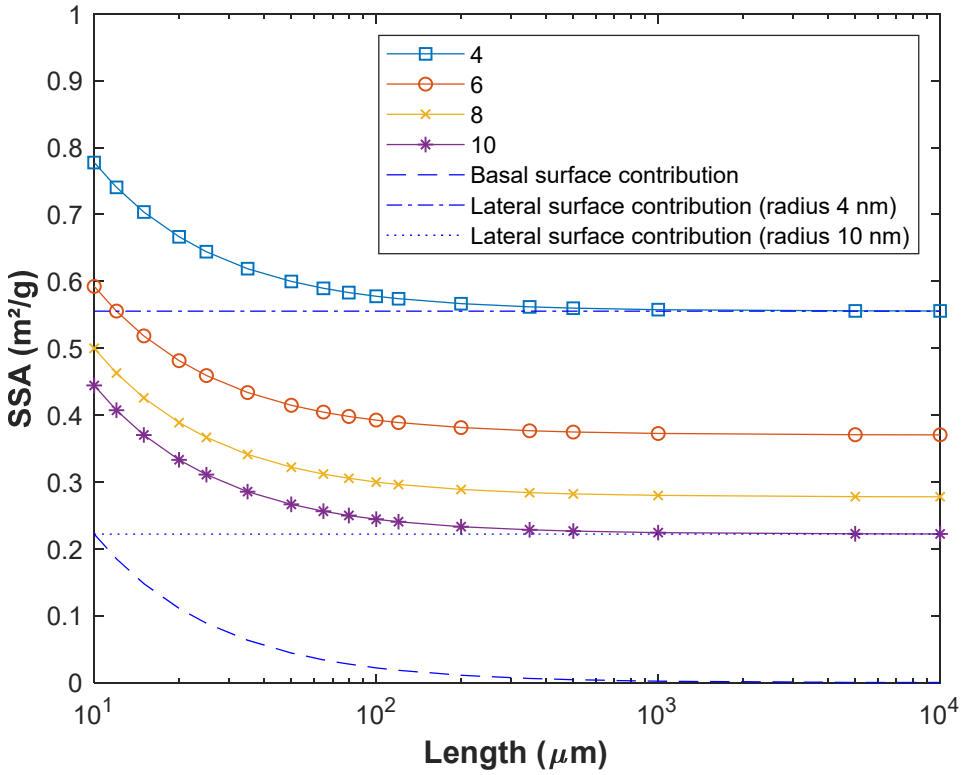

Figure G.1. Theoretical specific surface areas (SSA) calculated for cylinders with different radii (*R*) in the range 4 to 10 µm (indicated). SSA is reported as a function of the cylinder length (*L*). The total SSA of a cylinder is the sum of two components. The first contribution corresponds to the 2 basal surfaces and is proportional to 2/*L*, and the second one corresponding to the lateral surface is proportional to 2/*R*.

H. Complementary electrophoretic mobility results.

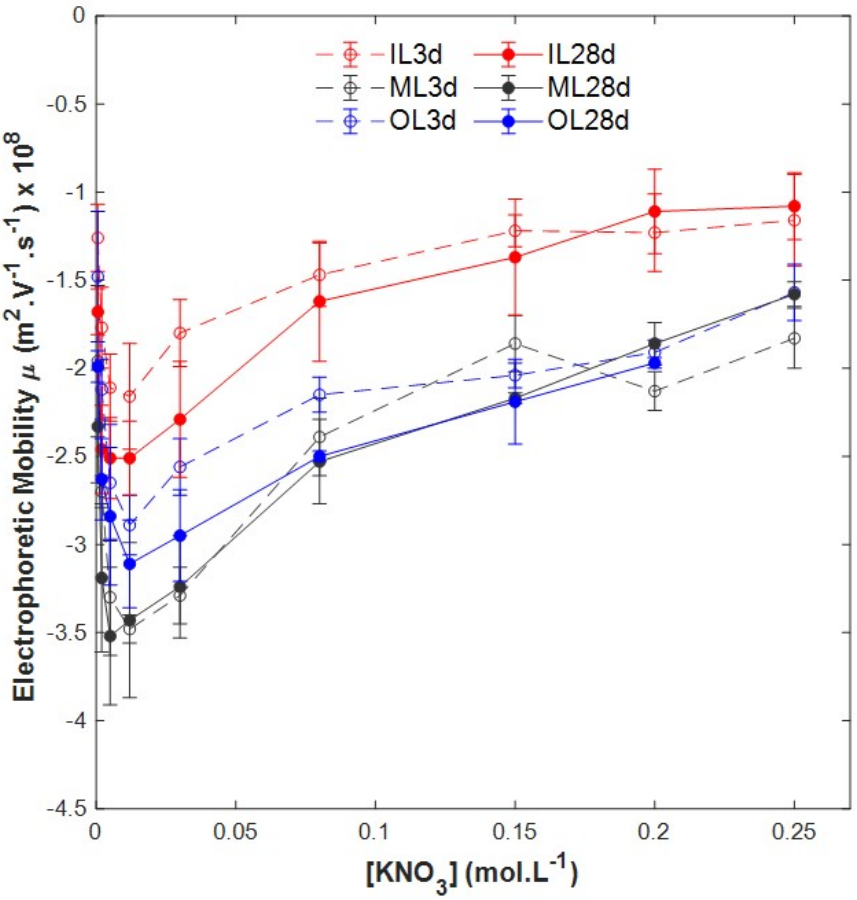

Figure H.1. Electrophoretic mobility measured on masks debris (specified) as a function of KNO_3 concentration at pH 7.35. IL: inner layer, ML: middle layer, OL: outer layer. 3d, 28d: after 3 days and 28 days UV-exposure, respectively. Data correspond to those reported in Figure 3A and are plotted here according to linear scale in KNO_3 concentration.

I. Characterization of nanoparticles released from polypropylene granulates.

Additional photodegradation experiments were carried on polypropylene (PP) beads purchased from GOOVEAN FIBERS Ltd (https://goonveanfibres.com/). The received granulates of 90 µm size were poured in a crystallizer so as to cover its surface and then placed under a UV lamp (Benda, at 366 nm, 6 W). The exposure protocol consisted in 7 cycles of 24 hours with alternating 16 hours UV radiation followed by 8 hours in dark. After exposure, 56 mg of granulates were dispersed in 350 mL of very soft water prepared by adding 24 mg of $NaHCO_3$, 15 mg of $CaSO_4$ and $MgSO_4$, 1 mg of KCl to 2 L of ultra-pure water with a conductivity of 0.055 $\mu S.cm^{-1}$. After one hour agitation, the smallest colloidal fraction was collected by filtering the suspension with glass fibre filters of 0.7 µm. The size of the nanoparticles and their electrophoretic mobility were measured by Dynamic Light Scattering and Phase Analysis Light Scattering techniques, respectively, both run with a Nano-ZS Malvern Instrument. Measurements were done with increasing KNO_3 concentration along the lines detailed in Materials and Methods section relative to the electrokinetic characterization of masks debris by electrophoresis. Electrophoresis and size results are provided below in **Figures I.1** and **I.2**, respectively.

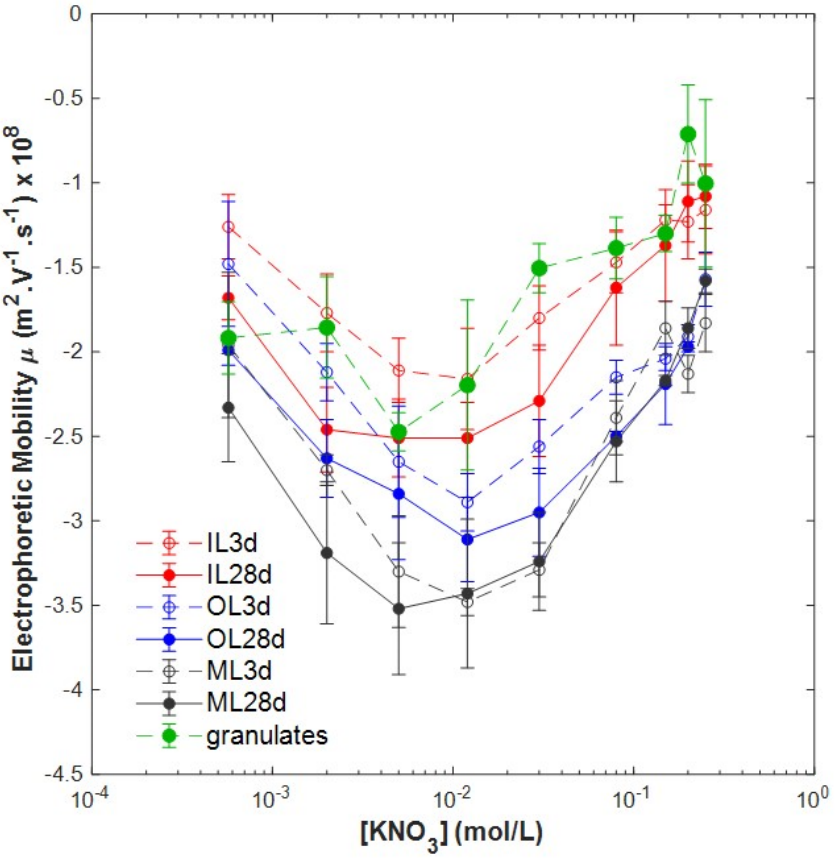

Figure I.1. Electrophoretic mobility measured on masks fragments as a function of KNO_3 concentration at pH 7.35. IL: inner layer, ML: middle layer, OL: outer layer. 3d, 28d: after 3 days or 28 days UV-exposure, respectively. The green curve corresponds to measurements performed on the filtered (<0.7 µm) fraction of a suspension of PP granulates recovered after dispersion in water of 90 µm beads exposed to UV for 7 days. Error bars correspond to triplicate measurements.

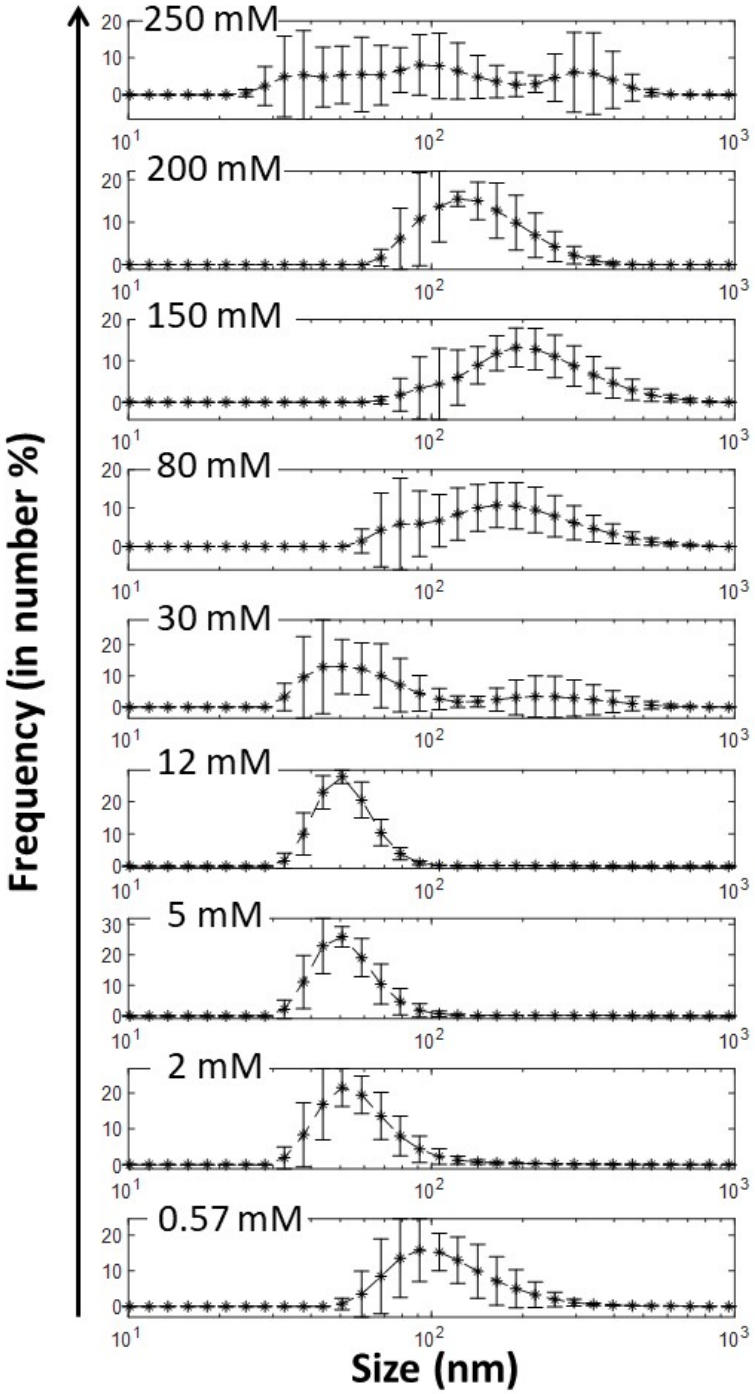

Figure I.2. Particle size distributions (expressed in number %) obtained by Dynamic Light Scattering (DLS) on the filtered (<0.7 µm) fraction of a PP granulates suspension after dispersion in water of 90 µm beads exposed to UV for 7 days. Each distribution corresponds to a green point in Figure I.1., i.e. a different concentration of KNO_3 (indicated). Error bars correspond to triplicate measurements.

J. Determination of the amount of released carboxylic acids by ion chromatography.

To determine the amount of carboxylic acid release in water by UV exposed mask layers, 18 mg of each layer UV-aged for 3 days and 28 days were dispersed in a bottle filled with 80 mL of very soft water. Bottles were left on a shaking table under natural light condition at room temperature for 3 months. Regularly, a volume of 2 mL was collected (i.e. after 1 h, 5 h, and 1, 2, 4, 7, 46, 58 and 91 days). The sampled solutions were then analysed using a compact high-pressure ion chromatography system (ICS-5000+ - Thermo), coupled with an ISQ EM single quadrupole mass spectrometer. Results are provided below in **Figure J.1**.

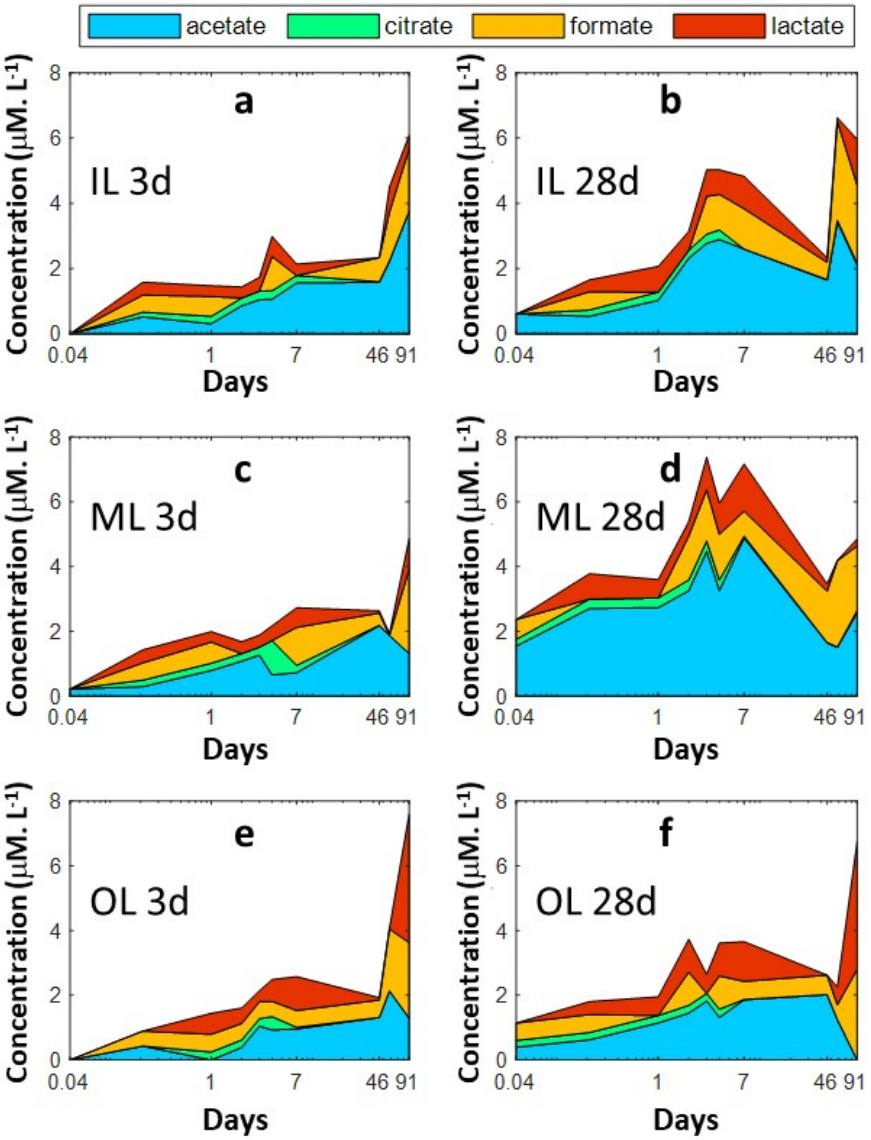

Figure J.1. Determination of the amount of carboxylic acids (from acetate, citrate, formate and lactate, as specified) released in solution by UV-aged masks debris under agitation condition (maximum duration of agitation: 91 days). IL: inner layer, ML: middle layer, OL: outer layer. 3d, 28d: layers after 3 days or 28 days UV-exposure, respectively.

K. Analysis of bacterial community composition in freshwater biofilms grown on masks.

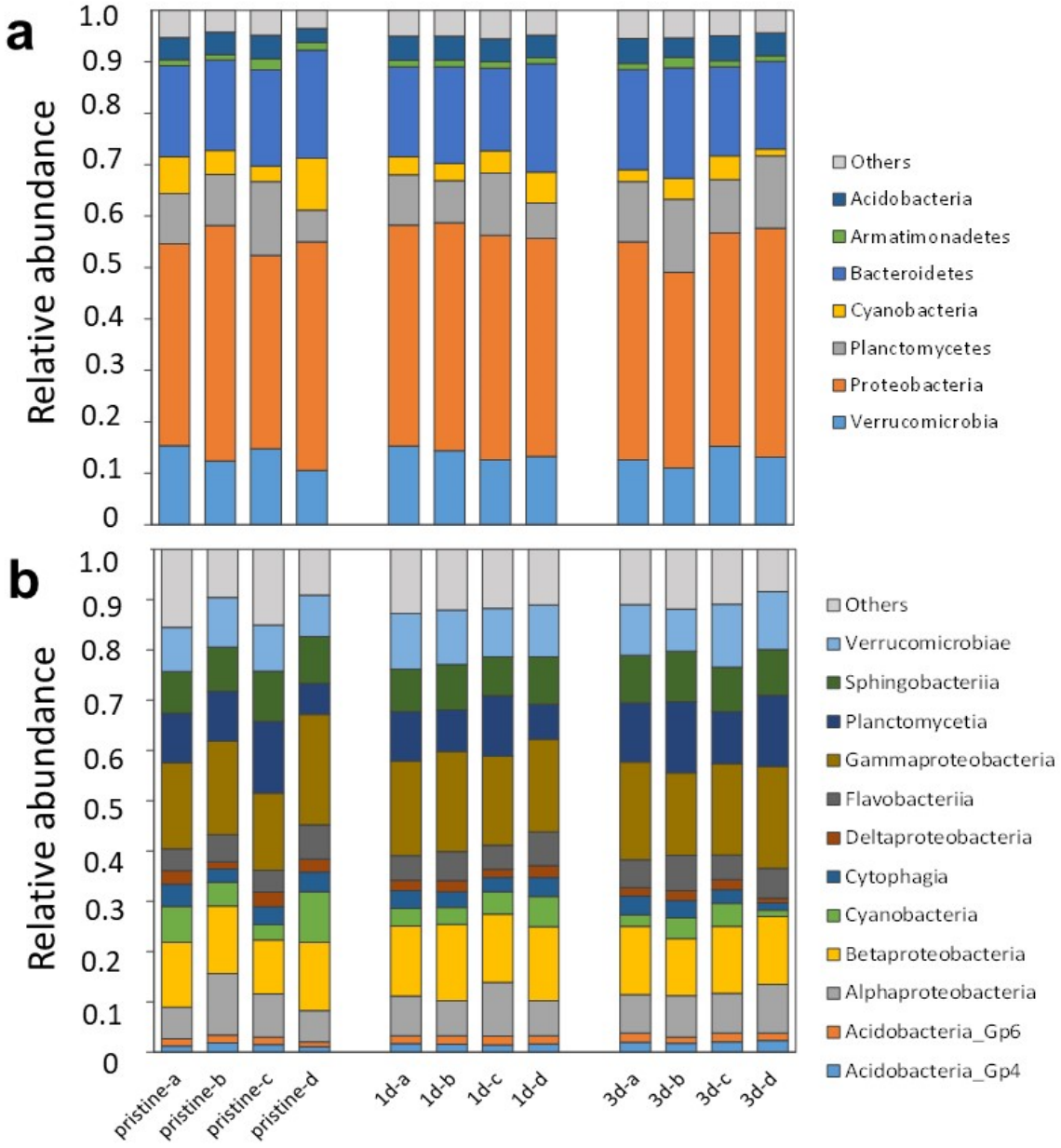

Figure K.1. Bacterial taxonomic distribution at the phylum **(a)** and class **(b)** levels. Pristine: no exposure; 1d, 3d: masks after 1 day and 3 days UV-exposure, respectively. For each condition tested, 4 independent replicates are analysed and reported here (designed by the letters a, b, c, d).

L. Analysis of phytoplankton community composition in freshwater biofilms grown on masks.

Table L.1. Relative abundance of Bacillariophytes (diatoms), Chlorophytes and Cyanophytes in biofilms.

	Pristine-a	Pristine-b	Pristine-c	1d-a	1d-b	1d-c	3d-a	3d-b	3d-c
Bacillariophytes									
Small pennate diatoms (*Achnanthidium* and others) - 10-11 µ	43	85	9	50	34	16	45	37	32
Gr. *Achnanthidium*	1	8	4	4	3	4	7	3	2
Gr. *Encyonema /Amphora*	3			16	10	1	18	7	13
Gomphonema spp.	5			5	7	2	7		
Humidophila					7				
Fragilaria	2								
Navicula		8				1			
Nitzschia	1					4			
Odontidium mesodon					7				
Planothidium				3	17	1			3
Pennate diatoms (connective vision)	1				7		2		7
Rhoicosphenia						3			
Chlorophytes									
Characium			24			4			
Chaetophorales (*Stigeoclonium* and others)	2		2			23			
Chlamydomonadales	19		10			22	3	3	
Ulotrichales (*Tetraciella*)			34			6			
Cyanophytes									
Chamaesiphon	0.5			1.2				15.5	1
Synechococcales (*Leptolyngbya*, *Heteroleibleinia*)	18.4		10	13.4		13.8	10.2	27.5	31.2
Pseudanabaena catenata	0.7				3.4	2.5			0.2
Others	2		7	6	6		8	6	9

M. Additional illustrative confocal microscopy images of freshwater biofilms grown on masks.

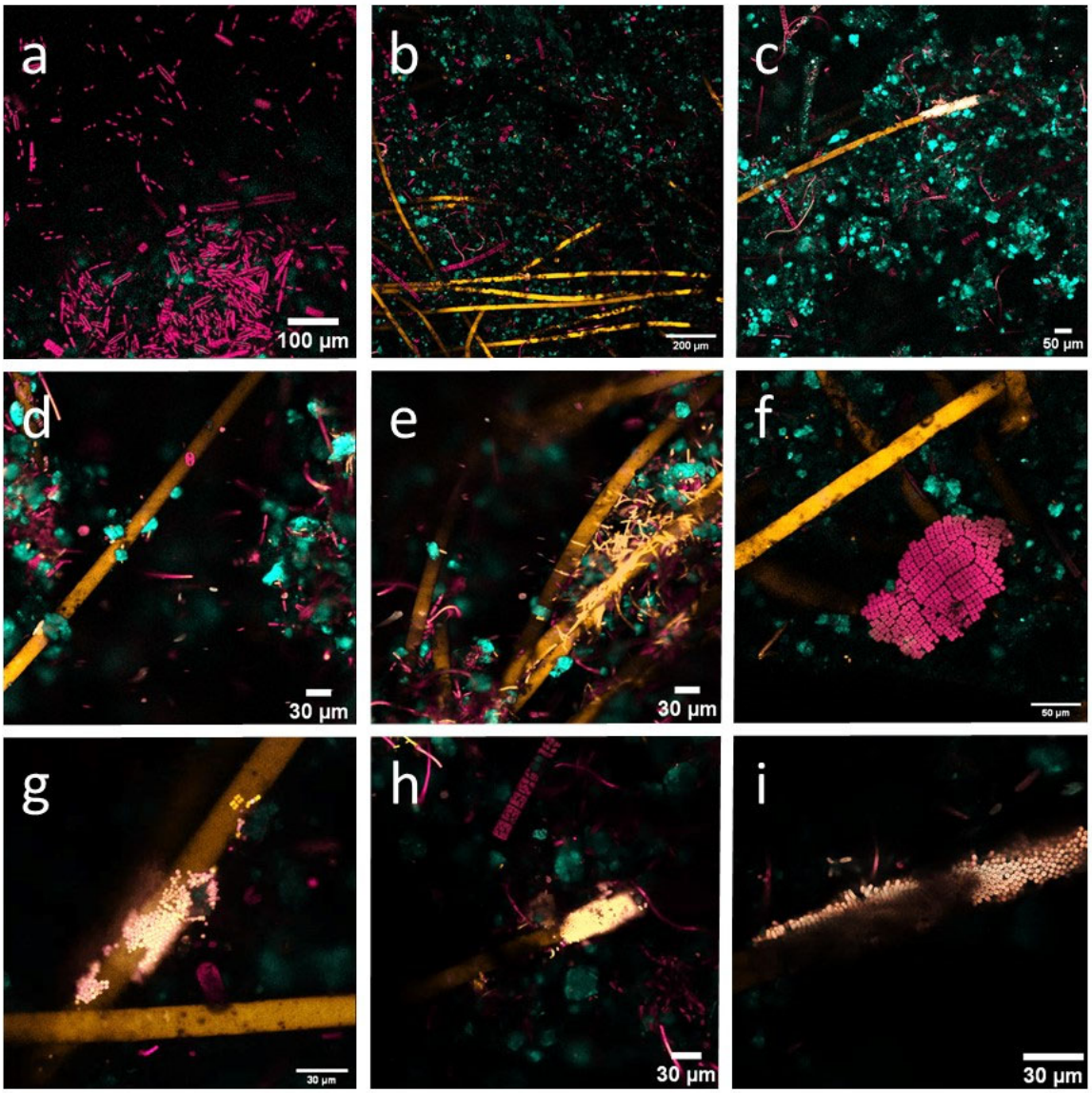

Figure M.1. Confocal laser scanning microscopy of freshwater biofilms developed on mask after a stay of 4 weeks in the Moselle River. Pictures are merged from the three channels used to collect autofluorescence (C1 – Exc 488 nm/Em: 499-561 nm, C2 – Exc 561 nm/Em: 570-632 nm, C3 – Exc 633 nm/Em: 641-694 nm). **(a)** Pristine mask, picture recorded on the coverslip focal plane. **(b)** 1d-mask. **(c)** 3d-mask. **(d)**,**(e)** Pristine mask. **(f)**,**(g)** 1d-mask. **(h)**,**(i)** 3d-mask. Pristine: no exposure; 1d, 3d: samples after 1 day and 3 days UV-exposure, respectively. The colour adopted for each channel corresponds to the median detection wavelength in that channel.

N. Observation of mineral deposits in the freshwater biofilm grown on masks.

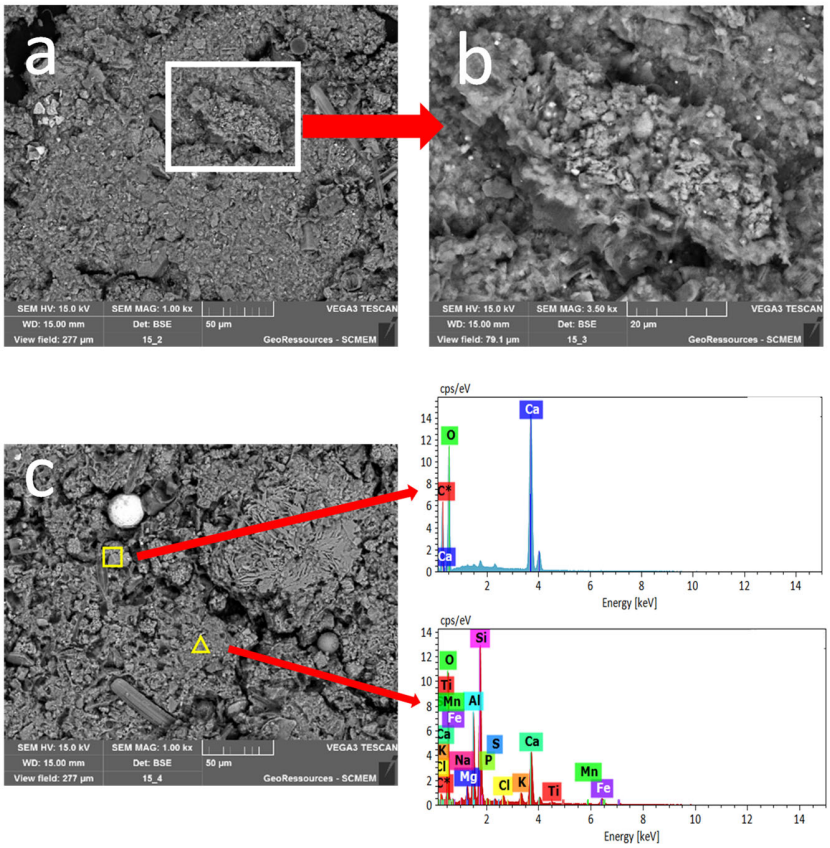

Figure N.1. Illustrative Scanning electron micrographs (SEM) of particles on a pristine mask after 4 weeks in the Moselle River. **(a)** Assembly of aggregates sampled on a pristine mask, **(b)** enlarged view of an aggregate, **(c)** elemental analysis by energy dispersive X-ray spectroscopy (EDS).

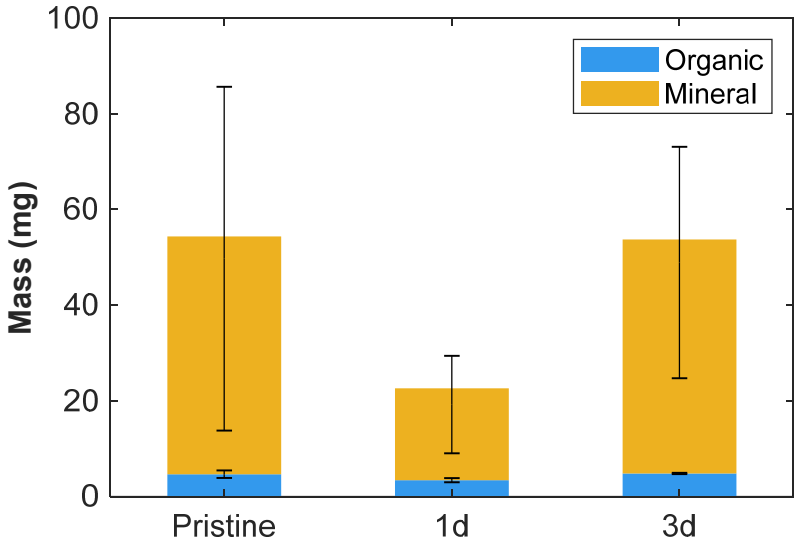

Figure N.2. Evaluation of organic and mineral mass after loss on ignition of masks incubated 4 weeks in the Moselle River. Experiments were performed to reveal the possible presence of mineral phases in the biofilms. The experimental procedure we followed was adapted from the protocol by Mathieu and Pieltain (2003). Briefly, 2 cm diameter disks cut from pristine, 1 day or 3 days-aged masks immersed for 4 weeks in Moselle River were first dehydrated for 16 hours at 220°C and then calcined for 4 hours at 450°C. Two replicates were averaged per condition.

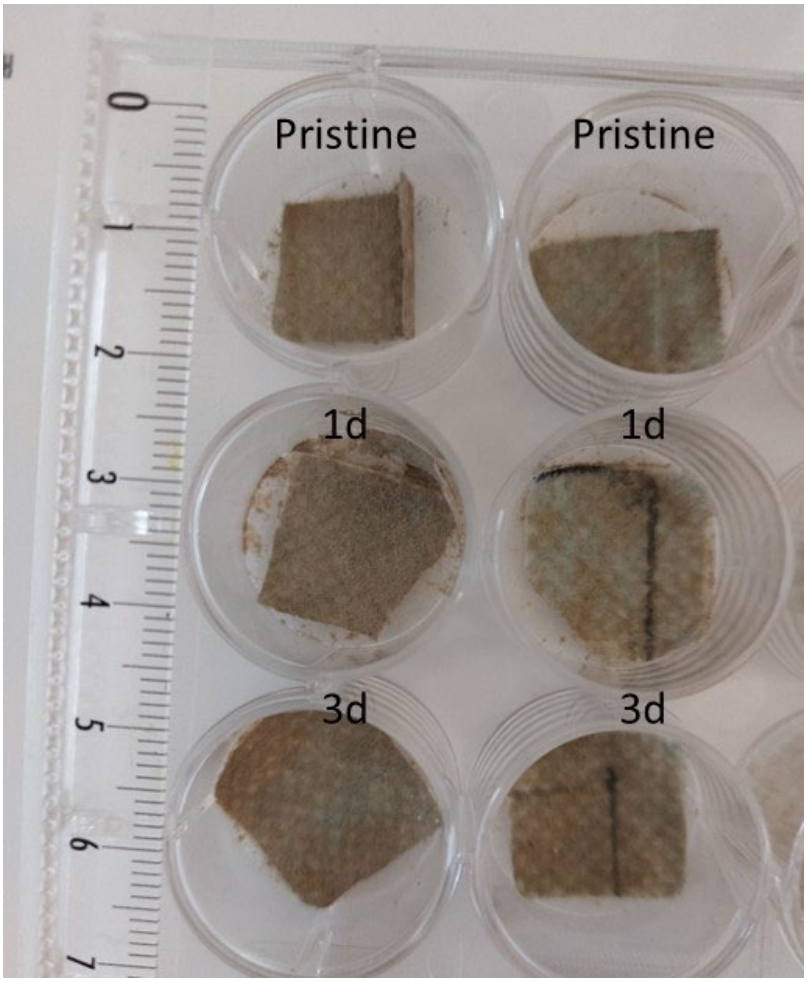

Figure N.3. Macroscopic view of masks incubated 4 weeks in the Moselle River. Mask pieces were placed in a multi-well plate for CLSM measurements.

O. References.

Brunauer, S., Emmett, P.H., Teller, E., 1938. Adsorption of Gases in Multimolecular Layers. *J. Am. Chem. Soc.* 60, 309–319.

Celina, M.C., Linde, E., Martinez, E., 2021. Carbonyl Identification and Quantification Uncertainties for Oxidative Polymer Degradation. *Polym. Degrad. Stab.* 188, 109550.

Mathieu, C., Pieltain, F., 2003. Analyse chimique des sols. Méthodes choisies. Tec & doc; Lavoisier, France.

Sing, K.S.W., 1985. Reporting physisorption data for gas/solid systems with special reference to the determination of surface area and porosity (Recommendations 1984). *Pure Appl. Chem.* 57, 603–619.

Wojdyr, M., 2010. Fityk: a general-purpose peak fitting program. *J. Appl. Crystallogr.* 43, 1126–1128.